SAND2007-3258C

Fuel Stratification for Low-Load HCCI Combustion: Performance & Fuel-PLIF Measurements

Wontae Hwang, John E. Dec, and Magnus Sjöberg
Sandia National Laboratories

ABSTRACT

Fuel stratification has been investigated as a means of improving the low-load combustion efficiency in an HCCI engine. Several stratification techniques were examined: different GDI injectors, increased swirl, and changes in injection pressure, to determine which parameters are effective for improving the combustion efficiency while maintaining NO_X emissions below U.S. 2010 limits. Performance and emission measurements were obtained in an all-metal engine. Corresponding fuel distribution measurements were made with fuel PLIF imaging in a matching optically accessible engine. The fuel used was iso-octane, which is a good surrogate for gasoline.

For an idle fueling rate ($\phi = 0.12$), combustion efficiency was improved substantially, from 64% to 89% at the NO_X limit, using delayed fuel injection with a hollow-cone injector at an injection pressure of 120 bar. Relative to this base case, changing to an 8-hole injector provided the single largest improvement, increasing combustion efficiency to 92%. The effects of swirl varied with injector type, but increased injection pressure was beneficial for both injectors. The highest combustion efficiency of 92.5% at the NO_X limit was achieved with the 8-hole injector and an injection pressure of 170 bar, with low swirl.

Quantitative fuel-distribution maps derived from the PLIF images showed good agreement with the combustion-efficiency and NO_X-emission measurements in the metal engine. The images showed that at the NO_X limit, fuel distributions and maximum equivalence ratios (ϕ) are similar for the two injectors, with delayed injection producing a single large fuel pocket. Fuel-mass histograms suggest that the 8-hole injector improved the combustion-efficiency at the NO_X limit by reducing the fraction of low-ϕ regions, but a wider field of view is required to fully confirm this. The images also show that increased swirl inhibited the mixing of fuel into the center of the combustion chamber, explaining the slower mixing rates observed in the metal engine. A general finding is that the combustion-efficiency/NO_X tradeoff improves when fuel can be injected as late as possible with acceptable levels of NO_X. Therefore, techniques that provide even faster mixing have the potential for further improvements.

INTRODUCTION

Homogeneous charge compression ignition (HCCI) combustion can provide high diesel-like efficiencies and very low nitrogen oxides (NO_X) and particulate emissions from internal combustion engines. However, there still remain several hurdles that must be overcome before this promising engine technology can become viable. Among these, improving combustion efficiencies and reducing emissions of carbon monoxide (CO) and hydrocarbons (HC) at low loads (idle to 2x idle fueling) must be properly addressed. A significant portion of the operating time is spent at these low loads, so improvements in combustion efficiency and emissions would have a significant impact.

In order to develop strategies to overcome this low-load problem, it is important to understand the cause of these low combustion efficiencies and high CO and HC levels. Figure 1 shows the trends of combustion efficiency and emissions plotted as a function of fuel/air-equivalence ratio (ϕ) for operation with a fully premixed mixture of iso-octane and air, at a compression ratio (CR) of 18 (taken from Ref. [1]). Data for a CR = 14 case, which will be explained later, are shown for comparison. The emissions are given as the percentage of total fuel carbon in each of the exhaust species to remove changes due solely to the quantity of fuel supplied. The 50% burn point (CA50) was held constant at top dead center (TDC). At intermediate loads where ϕ was increased beyond 0.2 (right of the dashed line in Fig. 1), CO and HC levels are low, and carbon dioxide (CO_2) levels are high, indicating good combustion. Indeed, the combustion efficiency is high, reaching about 95%. However, when ϕ was decreased below 0.2 (to the left of the dashed line), CO and HC levels start to rise rapidly while CO_2 levels sharply decrease, and the combustion efficiency drops to unacceptable levels of about 60% at diesel idling conditions ($0.11 \le \phi \le 0.13$). At these low loads the mixtures are dilute, so the combustion temperatures are too low (typically below 1500 K), and the bulk-gas reactions (particularly CO-to-CO_2 reactions) become so slow that they are quenched by the expansion before reaching completion [2-6].

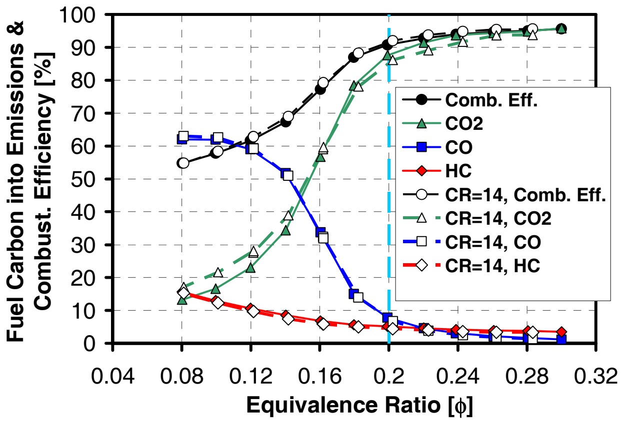

Figure 1. Combustion efficiency and emissions as a function of fuel loading for a fully premixed mixture of iso-octane and air at CR = 18 (from Ref. [1]). Data for CR = 14 are also shown for comparison. Operating conditions: 1200 rpm; P_{in} = 100 kPa for CR = 18 and P_{in} = 135 kPa for CR = 14; intake temperatures were set so CA50 = TDC.

Previous work has shown that fuel stratification using gasoline-type direct injection (GDI) can significantly improve low-load combustion efficiency [3,7,8]. Fig. 2 shows how the combustion efficiency and emissions change with fuel-injection timing of a hollow-cone GDI injector from early in the intake stroke at 20° crank angle (CA)[1] to well up the compression stroke (320°CA). A reference case that instead uses an external fuel vaporizer to provide a fully premixed mixture is plotted at start of injection (SOI) = 0°CA. Fueling of iso-octane was kept constant at an intake ϕ = 0.12, and CA50 was fixed at TDC by adjusting the intake temperature. Early injection essentially gives the same results as the fully premixed case, with a low combustion efficiency of 62% and high levels of CO and HC emissions. As injection timing is delayed beyond 90°CA, combustion efficiency starts to increase while CO and HC emissions start to decrease. Soot levels remain low. By retarding the injection timing, the time for fuel/air mixing is reduced, which creates local regions of higher in-cylinder ϕ that burn hotter, enabling the bulk-gas reactions to reach completion. This trend of improving combustion efficiency continues for all SOIs investigated. However, for SOIs later than 300°CA, the mixture becomes sufficiently close to stoichiometric in some regions that NO_X emissions rise rapidly due to increased combustion temperatures. By 305°CA, they exceed the U.S. 2010 indicated specific NO_X ($ISNO_X$) limit of 0.27 g/kWh. Hence, there is a tradeoff between combustion efficiency and NOx. Nonetheless, for the case in Fig. 2, delaying the fuel injection increased the combustion efficiency from 62% for the well-mixed cases to 87% with NO_X levels below the U.S. 2010 limits, as indicated by the black circles.

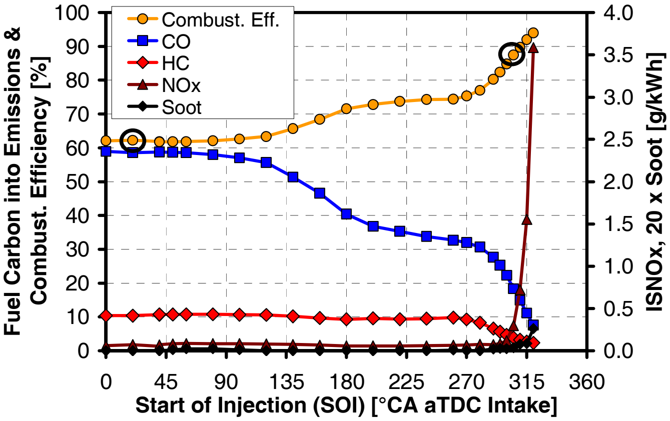

Figure 2. Combustion efficiency and emissions as a function of iso-octane injection timing for a hollow-cone GDI injector. Operating conditions: ϕ = 0.12; 1200 rpm; CR = 18; P_{in} = 100 kPa; intake temperatures were set so CA50 = TDC.

The ideal mixture, therefore, would be stratified in such a way that the minimum in-cylinder ϕ is higher than 0.2 (Fig.1) so combustion can reach completion, and the maximum in-cylinder ϕ is lower than about 0.6 so NOx formation is avoided.[2] Optical diagnostics provide means to visualize the fuel distribution, which gives us insight into methods for further improvement of the mixture preparation. Several studies have shown that chemiluminescence provides an indication of the inhomogeneities of HCCI combustion [9-14]. However, the chemiluminescent signal that is recorded is not a direct measurement of the fuel distribution in a given plane, but rather a line-of-sight integration of the combusting zones. Fuel planar laser-induced fluorescence (PLIF) can provide quantitative in-cylinder equivalence ratios of the mixture at a specific location, and is therefore a far more accurate measurement of the fuel distribution [9-11,15-21]. It is employed in the current study to investigate the different stratification techniques.

There are two main objectives to this work. First, we examine various fuel stratification techniques such as different GDI fuel injectors, injection pressures, and swirl in an all-metal engine to determine which parameters are effective for improving the combustion-efficiency/NOx tradeoff. Performance and exhaust emission measurements are obtained to identify techniques that improve the fuel/air mixture preparation. Second, we examine the fuel distributions for these various stratification techniques in a matching optically accessible engine. To accomplish this, an enhanced fuel PLIF diagnostic was de-

---

[1] 0°CA is taken to be TDC intake, so 360°CA is TDC compression.

[2] For the operating conditions studied here, the NO_x emissions typically remain below US 2010 emission standards as long as a majority (>95%) of the fuel is mixed to a ϕ lower than about 0.6. The selection of ϕ = 0.6 is based on NO_X measurements for well-mixed high-load operation, and on multi-zone modeling. However, the highest acceptable ϕ depends on several factors, such as combustion phasing, fuel-type, fueling rate, engine speed, EGR/residual level, and the specific fuel distribution. Therefore, ϕ = 0.6 is not a hard limit. Nonetheless, for the purpose of this study, it is beneficial to discuss the observed NO_x emissions in relationship to the amount of fuel located at ϕ higher than 0.6.

veloped that incorporates novel calibrations and temperature corrections. The fuel distributions are visualized using sequences of in-cylinder equivalence-ratio maps, and also statistically evaluated using probability density functions (PDFs) and histograms. This helps provide an understanding of the variations in performance that were observed in the metal engine.

Descriptions of the engine facility and data acquisition techniques are given in the next section. Following this, results of performance and exhaust emissions from the all-metal engine are presented and discussed. Next, results from the optical engine are given, starting with chemiluminescence images to provide a visualization of the changes in combustion with fuel stratification. This is followed by the fuel PLIF imaging results, which are the main subject of this section. In the final section of the paper, the findings are summarized and conclusions are drawn.

EXPERIMENTAL SETUP AND TECHNIQUES

ENGINE FACILITY

Matching single-cylinder all-metal and optically accessible research engines were used for the experiments. They were both derived from a Cummins B-series medium-duty, six-cylinder diesel engine, which has a displacement of 0.98 liters per cylinder with a 102 mm bore and 120 mm stroke. The two engines were mounted on either end of a double-ended dynamometer that can either motor the engines or absorb load to maintain a constant speed. A schematic of the engine facility is shown in Fig. 3a with one engine. Detailed descriptions of the facility and engines are given in previous studies [3,14], so only a brief description is presented here. Table 1 lists the specifications for these engines.

The engines were converted to single-cylinder HCCI research engines by deactivating cylinders 1 – 5 and installing custom HCCI pistons in cylinder 6. The pistons in the deactivated cylinders were retained for balancing, and their mass was adjusted to match the mass of the HCCI piston in cylinder 6. For the optical engine, this required the use of tungsten weights to compensate for the large mass of the extended Bowditch-type piston.

The combustion chamber was pancake-like for both engines. However, the metal-engine piston had a scallop in the central region to adjust the compression ratio, as can be seen in Fig. 3b. This was necessary because the height of the piston in the rim region could not be further decreased without getting too close to the top piston ring, which had a fixed position. The extended piston of the optical engine had a completely flat piston-crown window for optical access, thus creating a true pancake combustion chamber, as can be seen in Fig. 3c and Fig. 4. The spacer ring that forms the top part of the cylinder wall for the optical engine contained three windows. This allowed a laser sheet to pass through the cylinder to an

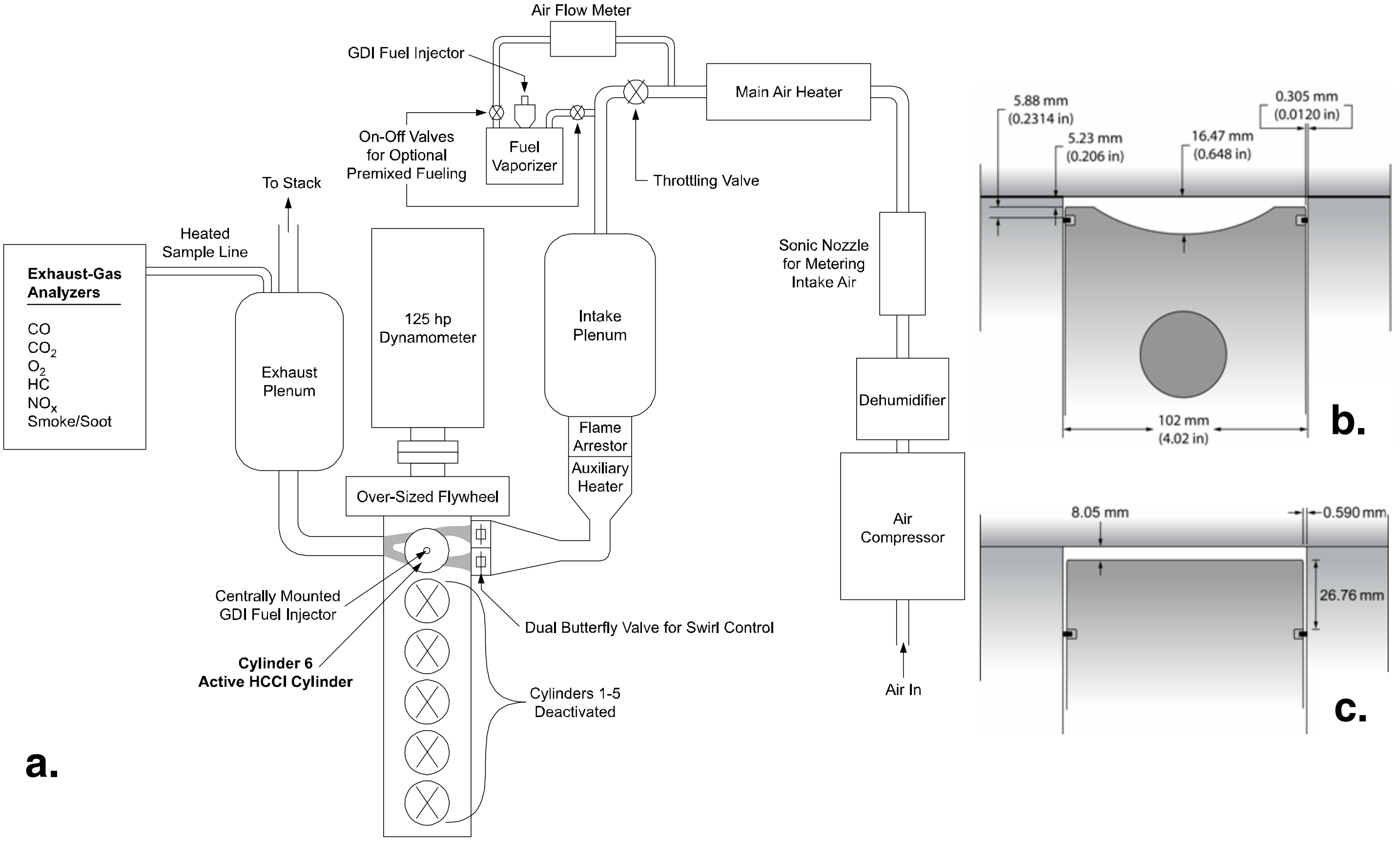

Figure 3. (a) Schematic of the HCCI engine facility. Only one engine is shown. The dynamometer can be coupled to either engine. (b) Schematic of the CR = 14 metal-engine HCCI piston and (c) optical-engine HCCI piston, both at TDC.

TABLE 1. Engine Specifications and Operating Conditions

Displacement (single-cylinder)	0.981 liters
Bore	102 mm
Stroke	120 mm
Connecting Rod Length	192 mm
Geometric Compression Ratio	14:1
No. of Valves	4
IVO	717°
IVC	205°
EVO	480°
EVC	8°
Engine Speed	1200 rpm
Intake Pressure	135 kPa
Coolant Temperature	100°C

external beam dump (Fig. 4). Like most optical engines, the top ring-land crevice is quite tall to prevent the rings from riding over the edge of the spacer-ring windows. The volume of the top ring land is accounted for in computing the geometric compression ratio. A drop-down cylinder liner with hydraulic-piston activation allowed rapid cleaning.

For most of this study, the geometric compression ratio (CR) was 14:1 for both engines.[3] Our previous low-load HCCI studies used CR = 18 at naturally aspirated conditions for iso-octane and gasoline [1,3,4,5]. Since we had switched to a CR = 14 piston for other studies, we decided to maintain this CR for the current study. The only exception is the chemiluminescence images, which had been previously acquired at CR = 18. With CR = 14 and an intake pressure (P_{in}) of 100 kPa, the intake heating system (which was limited to approximately 230°C) was not sufficient for low-load combustion of iso-octane. Thus, the intake pressure was boosted to 135 kPa, to match the TDC pressure of the CR = 14 cases to the CR = 18 cases. The intake temperature (T_{in}) was also set to match the TDC temperature of the CR = 18 cases, and was adjusted as necessary to maintain the 50% burn point at TDC. This required $140°C \le T_{in} \le 210°C$ for intake equivalence ratios from 0.28 to 0.08, respectively. (T_{in} for stratified operation will be discussed later.) With these adjustments, the combustion efficiency, CO, and HC levels for the CR = 14 data were nearly identical to the old CR = 18 data, as can be seen in Fig. 1. The slight difference in CO_2 was mainly the result of a new, more accurate CO_2 analyzer. The effects of stratification were also quite similar, as will be shown later.

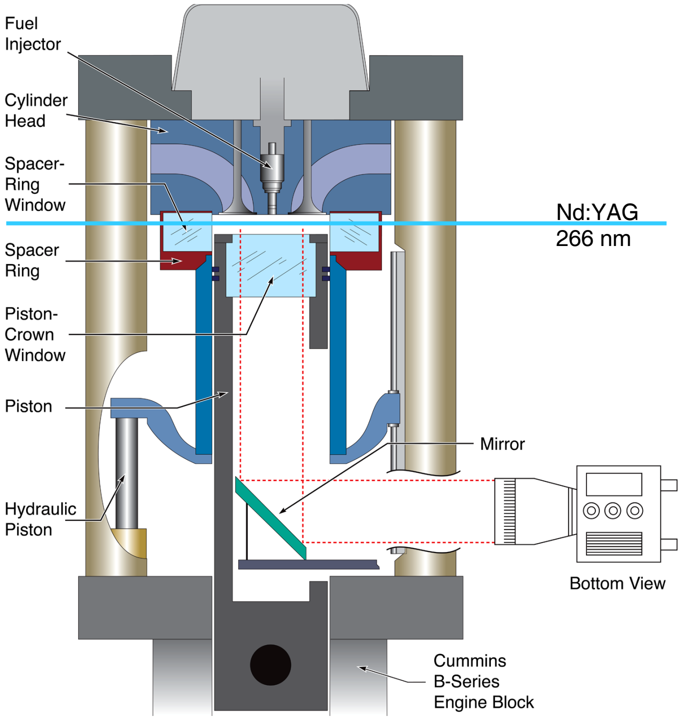

Figure 4. Schematic of the optically accessible HCCI research engine and PLIF setup.

The intake air was supplied by an air compressor, dehumidified to a dew point of 4°C by a refrigerated dryer, and electrically heated to the desired intake temperature. The air flow was metered and controlled by a sonic-nozzle orifice. Intake and exhaust plenums minimized pressure oscillations in the manifolds, and an auxiliary heater located close to the intake of each engine (see Fig. 3a) precisely controlled the intake temperature so the combustion phasing could be maintained at the desired crank angle.

The two intake ports were modified in the same manner for both research engines. Butterfly valves were installed on both ports (see Fig. 3a) to fully shut off the flow through either intake valve to control the swirl ratio (SR). Since the original production engine was designed to have high swirl, one of the intake ports was modified to incorporate an anti-swirl plate. This diverted the flow from the modified intake port to counteract the swirl generated from the other tangential intake port. As a result, when both butterfly valves were maintained in the fully open position, a low swirl ratio (Ricardo swirl number) of 0.9 was obtained for the metal engine. The optical engine had a slightly higher SR of 1.3. When the butterfly valve in the modified port was kept fully closed and the valve in the tangential port was kept fully open, a high SR of 3.2 was obtained for the metal engine, and a slightly higher value of 3.6 was obtained for the optical engine. The differences in swirl ratios between the two engines are most likely due to small differences in the casts of the intake ports within the cylinder heads. However, the differences between the engines are small compared to the differences between the low-swirl and high-swirl cases.

For most data in this study, fuel was supplied by a gasoline-type direct injector (GDI) mounted in the center of the cylinder head. Two injectors were evaluated, an axi-symmetric swirl-stabilized, hollow-cone spray injector and an 8-hole injector (Fig. 5). The hollow-cone injector that was used for the optical-engine experiments had a 54° cone angle. For the metal-engine experiments, the

---

[3] It should be noted that the valve pocket and head gasket crevices, which are not shown in Figs. 3 (b) and (c), contribute to the TDC volume, making the actual CR = 14.

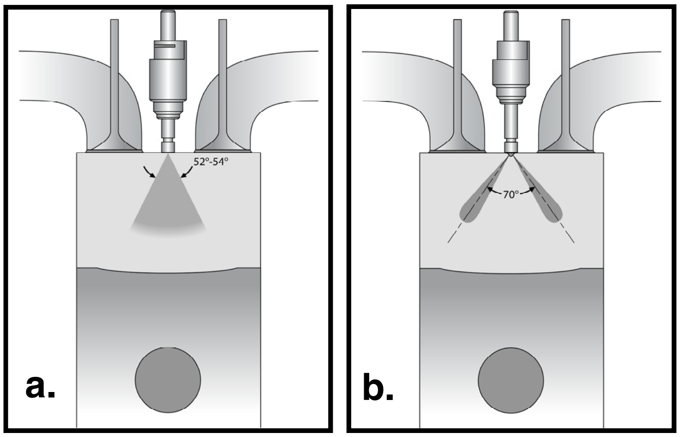

Figure 5. Schematic of the (a) swirl-stabilized hollow-cone and (b) 8-hole GDI injectors.

same type of injector was used, but it had a slightly different cone angle of 52°. The sprays of the 8-hole injector had a 70° included angle (Fig. 5b). A fully premixed fueling system utilizing an electrically heated fuel vaporizer was used to provide a well-mixed reference mixture for the performance and emission measurements, and uniform fuel distributions for calibration of the fuel PLIF diagnostic. A positive displacement fuel-flow meter was used to determine the amount of fuel supplied.

ENGINE OPERATION

Prior to running, the engine was preheated to 100°C by electrical heaters on the "cooling" water and lubricating oil circulation systems, and this temperature was held steady during the experiments for both engines. For this study, all data were taken at an engine speed of 1200 rpm and the intake air flow was adjusted to obtain a boosted intake pressure of 135 kPa. The metal engine was fired continuously with direct fuel injection, or sometimes with the premixed fuel vaporizer. The optical engine used DI fueling in a 11/1 skipfire mode (11 motored cycles followed by 1 fired cycle), originally to prevent overheating [14]. However, because the fuel tracer, toluene, had fluorescence quenching problems due to oxygen (which will be discussed later), the engine was eventually run inert with nitrogen (N_2) instead of air. Because of the 11 "non-fired" cycles, the residuals (~7% by mass) for the "fired" cycle consisted only of N_2 in the optical engine. The intake equivalence ratio, ϕ_{in}, was determined from the air and fuel flow rates, and was maintained at 0.12. The local equivalence ratio in the cylinder varies, and will be simply denoted as ϕ hereon. Since there is no O_2 present for the inert and non-combusting optical experiments, ϕ cannot be traditionally defined based on combustion stoichiometry. Therefore, the ratio of mass flow of fuel and N_2 for the non-combusting operation was kept the same as the corresponding ratio of fuel and air flow for operation with combustion. As such, the ϕ measured in cylinder for an inert case corresponds directly to that of a combusting case. The same global thermal conditions (intake-air, water, and oil temperatures) as the metal engine were maintained for the optical engine, so if there had been combustion, the phasing would have been at CA50 = TDC.

CONVENTIONAL DATA ACQUISITION

Cylinder pressure measurements were made with a piezoelectric transducer (AVL QC33C) at ¼°CA increments. The measurements were pegged (adjusted to match) to the intake pressure near bottom dead center (BDC) where the cylinder pressure reading was virtually constant for several degrees. For all data presented, 0°CA is defined as TDC at the start of the intake stroke (so TDC compression is at 360°). This eliminates the need to use negative crank angles or combined BTDC, ATDC notation.

For the actual fired conditions in the metal engine, the combustion phasing was controlled by first computing the apparent heat-release rate (AHRR) from the cylinder-pressure data (after applying a 2.5 kHz low-pass filter [3]). The AHRR was then used to determine the combustion phasing, which was defined as the 50% burn point (CA50) of the cumulative AHRR. Computations were performed for each individual cycle, disregarding heat-transfer and assuming a constant ratio of specific heats [22]. The average of 100 consecutive individual-cycle CA50 values was then set to the desired combustion phasing by adjusting the intake temperature.

Because the AHRR is the difference between the heat released and losses due to heat transfer, it does not always provide an adequate estimate of the actual heat-release rate (HRR) [1]. This is especially important when the HRR is small relative to the heat transfer rate, such as at the beginning and end of combustion. Therefore, when comparing the HRR for different conditions, the HRR was calculated using a more accurate method, which used the Woschni heat-transfer correlation [22]. The temperature dependence of the heat capacity of the gases was also taken into account. The heat release was calculated from the low-pass filtered ensemble-averaged pressure of 100 cycles.

Exhaust emissions data were also acquired after the engine operation had stabilized, with the sample being drawn from the exhaust plenum using a heated sample line (see Fig. 3a). For all conditions, the levels of CO, CO_2, HC, NO_X, and O_2 were measured using standard exhaust-gas analysis equipment. Smoke measurements were made with an automated smoke meter. However, smoke levels were zero or near-zero for all conditions studied, and are not presented except in Fig. 2.

FUEL

Iso-octane was chosen as the fuel for this study for several reasons. Since this study examines different fuel stratification strategies, the fuel must exhibit single-stage ignition characteristics so phasing advance is minimized with stratification [1]. Iso-octane is a single-stage ignition fuel in the operating range of interest, and it is also a good surrogate fuel for gasoline [1,4]. Also, it does not fluoresce with UV excitation, unlike gasoline, which has multiple fluorescing constituents. This is imperative for tracking the fuel distribution using PLIF. Liquid fuel and tracer must also co-evaporate so the tracer can properly track vaporized fuel molecules. Iso-octane co-evaporates fairly well with the common fuel tracers, toluene and 3-pentanone, because their boiling points and heats of vaporization are similar to iso-octane [16].

FUEL-PLIF DIAGNOSTIC

Many aspects were considered during the process of developing the fuel PLIF diagnostic. An appropriate tracer had to be selected. The tracer concentration had to be low enough so that the fuel characteristics were not changed much and laser sheet attenuation across the medium was minimal, yet sufficiently high so adequate signal was obtained. The laser energy had to be limited to prevent damage to the windows. Finally, the temperature sensitivity of the PLIF signal had to be considered and corrections applied for temperature variations resulting from differences in fuel-vaporization cooling and compression heating. These considerations are elaborated in more detail below.

An ideal fuel tracer 1) should give strong LIF signal with minimal absorption at low concentration, 2) have a minimal effect on engine performance, 3) have known spectroscopic characteristics, and 4) co-evaporate with the fuel [17,18]. Two tracers, a ketone and an aromatic, were evaluated using an excitation wavelength of 266 nm. The ketone, 3-pentanone, fluoresces in the visible regime (350 – 550 nm), and was imaged with a 50 mm f/1.2 glass lens with a "sky light" filter. This filter was used to make sure ultra-violet (UV) light was not captured, and to prevent engine oil from fouling the camera lens. The aromatic, toluene, fluoresces in the UV regime (265 – 330 nm), and was imaged with a 45 mm f/1.8 fused silica camera lens with a 277 nm long-wave-pass (LWP) and UG5 UV-bandpass (mainly between 220 and 400 nm) filters. The 277 nm LWP filter blocked elastic scattering from the excitation laser. The UG5 filter eliminated undesired interference from visible and near-IR light emission, thought to be largely due to fluorescence of residual oil in the metal that was excited by scattered and reflected laser light.

The concentrations needed to obtain adequate signal levels with a laser sheet at 23 mJ/pulse were 10% (by volume of fuel/tracer liquid mixture) for the 3-pentanone and 2% for the toluene. The high concentration level needed for the 3-pentanone could introduce unacceptable changes to the overall fuel characteristics. Even with the higher concentration, the signal-to-noise ratio (SNR) for 10% 3-pentanone was significantly worse compared to 2% toluene, as it had both weaker signals (about 2x weaker than toluene) and stronger background noise. Thus, 2% toluene was chosen as the fuel tracer. However, a disadvantage for toluene is that the fluorescence is strongly quenched by oxygen. Therefore, the optical engine was operated inert with nitrogen instead of air in order to eliminate this effect. Since the goal of this study is to examine the fuel/air mixture prior to combustion, it is not necessary to fire the engine, making operation with nitrogen acceptable. The thermal conditions in the optical engine were matched with those of the metal engine, which was set for iso-octane autoignition with CA50 = TDC. This resulted in compressed-gas temperatures almost 100 K lower than the toluene autoignition temperature of 1150 K, so thermal decomposition of the toluene tracer should not be an issue.

The PLIF setup is shown in Fig. 4. The 4th harmonic of an Nd:YAG laser (266 nm) was used as the excitation source. The beam first passed through a positive spherical lens with a long focal length of f = 773 mm to create a shallow waist approximately 0.5 mm thick at the center of the combustion chamber. Then it passed through a negative cylindrical lens with f = -30 mm to make a horizontal sheet, and finally an iris to remove the tails at either end of the sheet. Thus, the laser power varied only about 50% over the sheet width. The final sheet width occupied the full width of the front spacer-ring window. The windows were designed to have the same inner and outer radii of curvature to prevent the window from becoming a lens. However, the windows were thick, so the focusing effect could not be completely eliminated, and the sheet width slightly converged, from 43 to 37 mm over the field of view in the cylinder. The laser sheet energy measured after the iris was 23 mJ/pulse. For most of the data presented, the sheet was positioned 4 mm below the firedeck (*i.e.*, the flat cylinder-head surface), which was the mid-plane of the CR = 14 pancake combustion chamber.

An intensified CCD camera, sensitive in both the visible and UV ranges, captured the toluene fluorescence through the piston-crown window at a resolution of 640 x 480 pixels. The 45 mm fused silica lens with the aperture set at maximum (f/1.8) was used with the 277 nm LWP and UG5 filters. The piston-crown window provides a field of view of 70 mm in diameter, which corresponds to approximately half of the area of the 102 mm diameter combustion chamber. For all images presented, a white circle around the imaged area shows the limits of the 70 mm field of view. The images were acquired at 365°CA, because this crank angle corresponds to the peak mass-averaged temperature for the fired engine when CA50 = TDC. Since the maximum NO_X formation rate will occur at this peak temperature, it is appropriate to image the mixture stratification at this point in the cycle and correlate it with the overall NO_X emissions.[4]

Conversion of the raw toluene PLIF images into quantitative equivalence-ratio images (ϕ maps) was accomplished using an advanced technique to correct the PLIF images for temperature differences resulting from fuel stratification. These occur due to the differences in vaporization cooling and thermodynamic properties associated with the fuel stratification. It is important to account

---

[4] It should be noted that, for fired conditions, as the high-temperature regions start to burn, they compress the unburned regions. This would slightly change the spatial fuel distribution. However, the statistical distribution of the fuel (*i.e.* the mass fractions at the various ϕ) does not change.

for this because the LIF signal is significantly increased by lower temperatures due to the large increase in fluorescence quantum yield [18,23]. Lower temperatures also result in higher mixture densities, which produce an additional small increase in the LIF signal. The diagnostic development is described in detail in Ref. [24], and only a brief description of the three main steps is given here.

First, the temperature sensitivity of the toluene LIF signal was quantified. A series of $\phi = 0.12$ premixed images were acquired at 365°CA for various intake temperatures. The temperatures at 365°CA were calculated by first computing the BDC temperatures using the method developed by the authors [25], and then assuming adiabatic compression from BDC following the measured pressure trace and using real-gas properties that were adjusted at each time step. For a temperature increase of 100 K near 1000 K at 365°CA, the toluene LIF signal was found to decrease by 30%.

Second, a premixed ϕ calibration was performed to obtain a relationship between ϕ and LIF signal. A series of premixed images at different ϕ, ranging from 0.12 to 1.0, were acquired at 365°CA. Although laser-sheet attenuation across the images is minimal for the low $\phi = 0.12$ stratified images, a correction was required for the well-mixed high-ϕ calibration images. The high-ϕ mixtures also had lower γ (ratio of specific heats), which leads to lower compression temperatures and higher LIF signals. A correction was applied for this using the temperature dependence of the toluene LIF signals obtained in the first step. The reference temperature was set at 1055 K, which corresponded to the compressed-gas temperature at 365°CA for $\phi = 0.12$. A linear relationship between ϕ and LIF signal was obtained after these two corrections. However, the stratified ϕ maps obtained using this relationship alone do not take into account the temperature differences resulting from the fuel stratification. Thus, a third step is needed.

Third, the temperature and ϕ at 365°CA for each fuel-mixture region of the stratified fuel image were computed iteratively, using the temperature and ϕ calibrations from the first two steps. This was done by first obtaining an initial estimate of the ϕ distribution, by assuming a uniform temperature at 365°CA and applying only the ϕ calibration (step two). Then, the temperature field at 365°CA was recomputed in three steps. 1) N_2 was adiabatically compressed along the experimental pressure trace until the crank angle of SOI for the image of interest. 2) It was assumed that the fuel was instantaneously injected, vaporized, and adiabatically mixed at the crank angle of SOI. The temperatures for the various ϕ regions were computed accounting for the vaporization cooling. 3) Each ϕ region was adiabatically compressed along the experimental pressure trace, using real-gas properties with a new γ at each time step. Because the high-ϕ regions have a lower γ, the compression heating is less, which further amplifies the temperature spread in the charge. Overall heat transfer was accounted for through the use of the measured pressure trace. Since both vaporization cooling and less compression heating act to reduce the temperature of the high-ϕ regions, the temperatures at 365°CA monotonically decreased with increasing ϕ. Using this computed temperature field, new ϕ estimates were made, and the process was repeated until converging on a unique solution for the ϕ and temperature corresponding to each image intensity value. In this manner, the temperature-corrected stratified ϕ maps and ϕ-corrected temperature maps are simultaneously obtained.

Several basic corrections were applied to the raw PLIF images before performing the temperature correction discussed above. The camera intensifier gain was changed for each condition, and was thus normalized against a reference gain using a calibration curve. The laser energy varied slightly from shot to shot, so the energy of each pulse was measured and normalized against a reference value. Even when there were no tracers in the cylinder, faint outlines of the valve pockets could be viewed in the background images, thought to be due to fluorescence of residual oil in the metal that was excited by scattered laser light. To correct for this, the average background image obtained from 20 non-fueled motored cycles was subtracted from the PLIF image. Camera and laser-sheet non-uniformities that were consistent from shot to shot were corrected for by normalizing the images with a reference flatfield image obtained at a premixed $\phi = 0.12$. After applying these basic corrections, maps of ϕ and temperature were obtained from a stratified fuel PLIF image, using the iterative technique described above. It should be noted that the in-cylinder pressure was nearly the same (less than 1% variation) for all the images, which were acquired at 365°CA, so any influence of pressure on the LIF signal can safely be neglected.

Correcting for the temperature differences arising from fuel stratification has a significant effect on the equivalence-ratio maps, as can be seen in Fig. 6. Figure 6a shows a raw PLIF image obtained at 365°CA with SOI = 305°CA for the hollow-cone injector. Figure 6b shows the ϕ map that is obtained after only the ϕ calibration in step two. Temperature corrections have not been implemented yet. The fuel-rich regions have a maximum ϕ of 1.3. Figure 6c shows the ϕ map that is obtained after using the iterative temperature corrections in step three. The overall amount of fuel appears greatly reduced, with the maximum ϕ levels dropping from 1.3 to 0.8. Thus, the corrected ϕ map in Fig. 6c has a 38% lower maximum ϕ than the non-corrected map in Fig. 6b. Ignoring this important temperature correction would have a significant impact on the usefulness of the ϕ maps. Figure 6d shows the temperature map that results from the fuel stratification. The temperature fluctuations that are observed are on the order of 100 K. This will have great implications on the sequential autoignition throughout the charge, and is important to consider when studying changes in the heat-release rate.

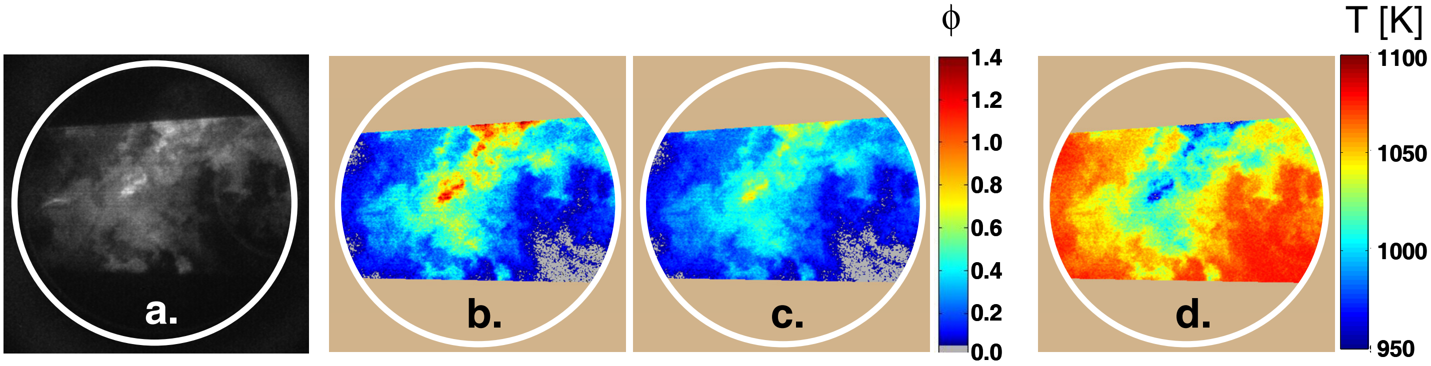

Figure 6. (a) Raw fuel PLIF image converted to (b) temperature-uncorrected equivalence-ratio map, (c) temperature-corrected equivalence-ratio map, and (d) temperature map. Hollow-cone injector with SOI = 305°CA. The white circle around each image shows the 70 mm diameter field of view through the piston-crown window.

PERFORMANCE AND EXHAUST EMISSION MEASUREMENTS IN THE METAL ENGINE

For the performance and exhaust emission measurements in the metal engine, fueling was maintained at ϕ_{in} = 0.12, corresponding to that of idle operation. The combustion phasing was maintained at CA50 = TDC by adjusting the intake temperature. Several techniques were investigated to improve the combustion-efficiency/NO_X tradeoff. The text matrix is given in Table 2. Two GDI injectors were evaluated: a swirl-stabilized hollow-cone injector with a cone angle of 52°, and an 8-hole injector. For each injector, the effects of two parameters, in-cylinder air swirl and fuel injection pressure (P_{inj}), were examined separately. The base condition for this study, highlighted in Table 2, was selected to be the hollow-cone injector at low swirl (SR = 0.9) and P_{inj} = 120 bar. The effects of swirl were examined by increasing the SR from the baseline value of 0.9 to a high value of 3.2. The effects of injection pressure were first examined by decreasing P_{inj} from the baseline value of 120 bar to 70 bar for both injectors. Then, the P_{inj} was increased to 170 bar for only the 8-hole injector, because the hollow-cone injector was not designed for such high injection pressures. For each technique in Table 2, the fuel stratification was varied by delaying injection from early in the intake stroke until well up the compression stroke. Data are presented in terms of SOI, but the results would be only slightly different if presented in terms of the end of injection, since the injection durations were only 0.4 ms (2.9°CA) and 0.63 ms (4.5°CA) for the hollow-cone and 8-hole injectors, respectively, at the fueling rate used (ϕ_{in} = 0.12) and P_{inj} = 120 bar.

TABLE 2. Test Matrix

	Hollow-cone	8-hole
P_{inj} = 70 bar	X	X
P_{inj} = 120 bar	X	X
P_{inj} = 170 bar		X
High swirl (SR = 3.2) P_{inj} = 120 bar	X	X

STRATIFICATION USING HOLLOW-CONE INJECTOR

Base Case – Combustion efficiency and emissions with varying injection timing are shown in Fig. 7a for the hollow-cone injector at the base condition. The trends are very similar to those in Fig. 2, which were for CR = 18, P_{in} = 100 kPa, and a slightly larger injector cone angle of 54°. Early injection at 40°CA gives results that are essentially identical to the fully premixed reference case plotted at SOI = 0°CA. For such well-mixed operation, the combustion efficiency was only 64%, and high levels of CO and HC emissions were detected.[5] This is due to the bulk gas temperature being too low to achieve complete combustion at this low equivalence ratio of 0.12, as discussed in the introduction. The gross indicated mean effective pressure (IMEPg) in Fig. 7b was stable at 56 kPa. As SOI is delayed beyond 90°CA, combustion efficiency and IMEPg start to increase while CO and HC emissions start to decrease. The standard deviation of the IMEPg[6] increases as well, indicating greater cycle-to-cycle variation due to the randomness in the stratification [3], but it remains within acceptable limits. After 240°CA, the increase in combustion efficiency and IMEPg and the drop in CO and HC levels become much more rapid. The standard deviation of the IMEPg begins to decrease, indicating less cyclic variability as the charge becomes highly stratified. It is noteworthy that the CO, combustion-efficiency, and IMEPg curves flatten temporarily from 210°CA to 240°CA, rather than showing a smooth progression with SOI as might be expected if the reduced time available for mixing were the only effect of

---

[5] The slightly higher combustion efficiency compared to the CR = 18 case in Fig. 2 is attributed to the larger volume-to-surface ratio for the larger clearance volume with CR = 14, which results in a slightly higher average combustion temperature and proportionally less HC from incomplete combustion in the top ring-land crevice.

[6] The percentage-base standard deviation of the IMEPg has been corrected for the heat transfer losses of a motored cycle. Thus, the definition is: Std. Dev. IMEPg [%] = 100 * Std. Dev. IMEPg / ($IMEPg_{fired}$ – $IMEPg_{motored}$).

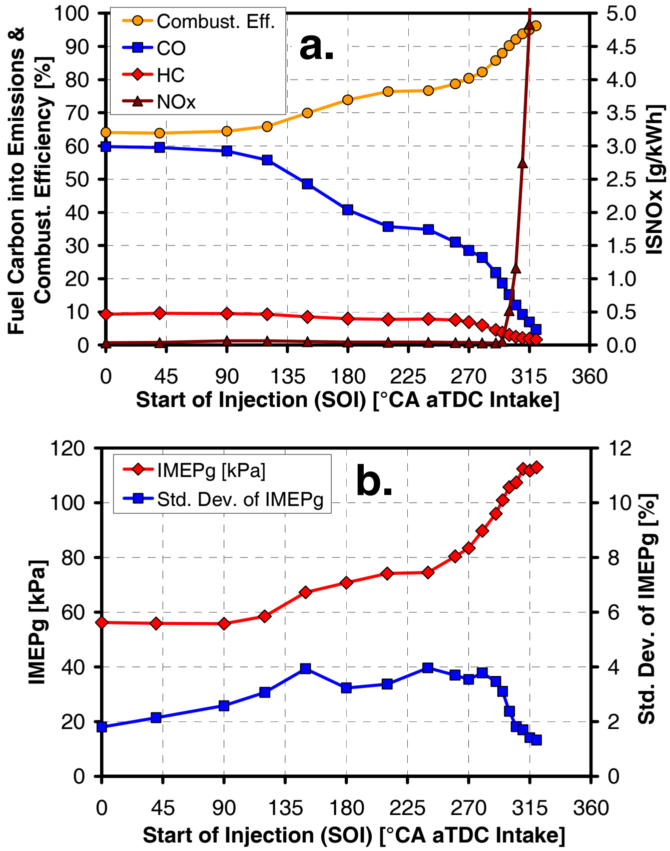

Figure 7. The effect of varying the start of injection for the 52° hollow-cone injector on (a) combustion efficiency and emissions and (b) IMEPg and standard deviation of IMEPg. Base condition with low swirl (SR = 0.9) and P_{inj} = 120 bar. Operating conditions: ϕ = 0.12; 1200 rpm; CR = 14; P_{in} = 135 kPa; intake temperatures were set to obtain CA50 = TDC.

retarding injection timing. This is most likely the result of changes in the mixing rate due to a partial collapse or structural change of the hollow-cone spray pattern when injecting into a higher density ambient as the piston gets closer to TDC, as has been observed for fuel sprays produced by similar hollow-cone fuel injectors [26].[7]

With retarded injection timing, the reduced mixing time, combined with any changes in the spray structure, result in local regions of higher ϕ that burn hotter, enabling the combustion reactions to reach completion. For an SOI of 295°CA or earlier, the NO_X emissions remain near zero. However, for SOIs later than 295°CA, NO_X emissions begin to rise rapidly. This suggests that the richest portions of the high-ϕ regions are becoming too rich, with a significant portion of fuel at $\phi > 0.6$, as will be examined with PLIF imaging later in this paper. The latest SOI for which the NO_X levels are still near zero (just before the rapid rise) is hereon referred to as the "NO_X knee". Thus, for this base case, the NO_x knee is at 295°CA. Shortly after the NO_X knee, the NO_X levels exceed the U.S. 2010 $ISNO_X$ limit of 0.27 g/kWh. Examination of the data shows that for this base case, delayed SOI can increase the combustion efficiency from 64 to 89%, corresponding to an increase in IMEPg from 56 to 103 kPa, while still maintaining NO_X levels below the U.S. 2010 limit. For this base case and all other stratification techniques examined, soot levels (not shown) remain very low even for late SOIs, well beyond the NO_X knee.

The intake-temperature requirements for this stratification technique are of interest. The intake temperature required to maintain CA50 at TDC is 205°C at SOI = 40°CA. At this early SOI, spray impingement onto the hot piston causes a large portion of the fuel vaporization. However, significant charge cooling still occurs, so the intake temperature needs to be 3°C higher than that of the premixed case [25]. As the injection timing is retarded, less heat for vaporization comes from the piston since there is less spray impingement, and the charge is cooled more by fuel vaporization. Fuel vaporization cooling continuously increases as the mixture becomes locally richer with delayed SOI, and the intake temperature needs to be increased up to 217°C at SOI = 210°CA. Beyond SOI = 210°CA, the intake temperature must be reduced because the local equivalence ratios become sufficiently high such that the fuel autoignition chemistry is enhanced [1]. At SOI = 295°CA (the NO_X knee), the intake temperature must be 205°C again.

Effects of Increased Swirl – The combustion-efficiency and emission trends for the hollow-cone injector high-swirl case (SR = 3.2) with P_{inj} = 120 bar are shown in Fig. 8. The overall trends are similar to the base case. However, there are some distinct differences. The swirl causes the increase in combustion efficiency and the decrease in CO and HC emissions from SOI = 120°CA to be more gradual. The NO_X emissions also start to rise at an earlier SOI, with the NO_X knee shifting to 285°CA. This indicates that more time is needed for sufficient mixing to occur so no rich NO_X-producing regions are present at the time of combustion. In other words, swirl slows the rate of fuel/air mixing, which perhaps seems a bit counter-intuitive.

It is difficult to see in Figs. 7a and 8 how the combustion efficiency at the NO_X knee changes compared to the base case, so the combustion efficiency is plotted directly against NO_X emissions in Fig. 9. As can be seen, the high swirl improves the combustion efficiency at the NO_X knee from 88% to 89%. Interestingly though, be-

---

[7] When injecting late into the compression stroke, piston wall wetting can occur under certain conditions. However, due to the high in-cylinder temperature, the liquid spray is vaporized rapidly. The in-cylinder pressure is also very high, so the jet penetration is reduced as well. Therefore, piston wall wetting is much more likely to occur for injection early in the intake stroke, when the lower in-cylinder temperatures and pressures allow the fuel to penetrate further. However, for all conditions examined in the current study, the intake temperature was very high, about 200°C. Therefore, iso-octane, which has a boiling point of 99°C, quickly vaporizes as it is injected. Even for conditions where some liquid fuel did reach the piston top, the surface was so hot that it would have immediately vaporized. Thus, wall wetting is not considered to be an issue for this study. This is confirmed by the nearly identical levels of HC, CO, NO_X, and soot emissions for the early SOI = 40°CA and premixed (shown as SOI = 0°CA) cases in Fig. 7 (a).

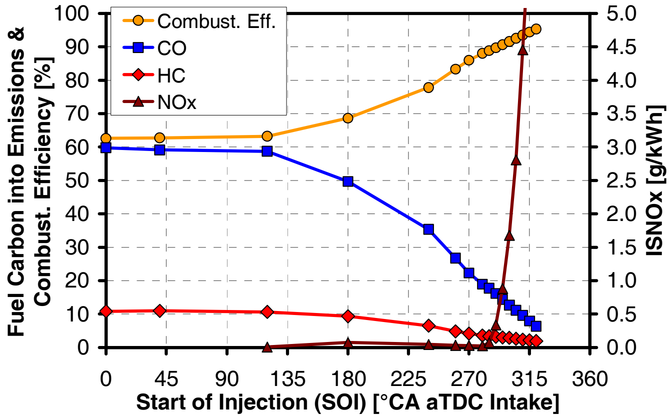

Figure 8. Combustion efficiency and emissions as a function of start of injection for the hollow-cone injector with high swirl (SR = 3.2) and P$_{inj}$ = 120 bar.

yond the NO$_X$ knee, the high-swirl curve in Fig. 9 has a steeper slope than the base case, *i.e.* NO$_X$ emissions increase more rapidly for a given change in combustion efficiency as SOI is retarded beyond the NO$_X$ knee for the high swirl case. As a result, at the U.S. 2010 limit, the combustion efficiency difference has narrowed to 0.5%.[8]

Effects of Injection Pressure – For the low injection pressure case with P$_{inj}$ = 70 bar, the general trends in combustion efficiency and CO, HC, and NO$_X$ emissions with SOI are very similar to those of the base case in Fig. 7a. The main difference is that the NO$_X$ knee is shifted about 15° earlier to SOI = 280°CA (not shown). This indicates a slower rate of fuel/air mixing, as could be expected from the lower injection velocities associated with the reduction of P$_{inj}$ from 120 to 70 bar. Since the decrease in CO and HC emissions with increasing SOI does not change greatly compared to the base case, this earlier NO$_X$ knee means that the combustion efficiency is reduced by about 2% at the NO$_X$ knee, as shown in Fig. 9.

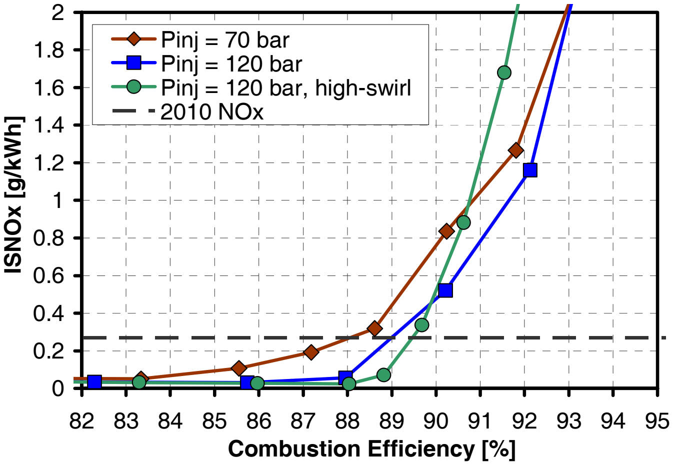

Figure 9. Effects of swirl and injection pressure on the combustion-efficiency/NO$_X$ tradeoff for the hollow-cone injector. The dashed line represents the U.S. 2010 NO$_X$ limit.

STRATIFICATION USING 8-HOLE INJECTOR

Comparison with Hollow-Cone Injector – Combustion efficiency and emission trends for the 8-hole injector at P$_{inj}$ = 120 bar and low swirl (SR = 0.9) are shown in Fig. 10. Unlike the hollow-cone injector, there is little change in the CO, HC, and combustion efficiency until the SOI reaches 210°CA. This means that the fuel and air remain well mixed until this relatively late SOI, indicating a much higher mixing rate with the 8-hole injector. This higher mixing rate also shifts the NO$_X$ knee to 315°CA, which is 20° later than that of the hollow-cone injector base case in Fig. 7a. Compared to this large shift in the SOI of the NO$_X$ knee, the combustion-efficiency rise is not retarded as much. This results in a significantly improved combustion-efficiency/NO$_X$ tradeoff, as can be seen in Fig. 11. The combustion efficiency is increased

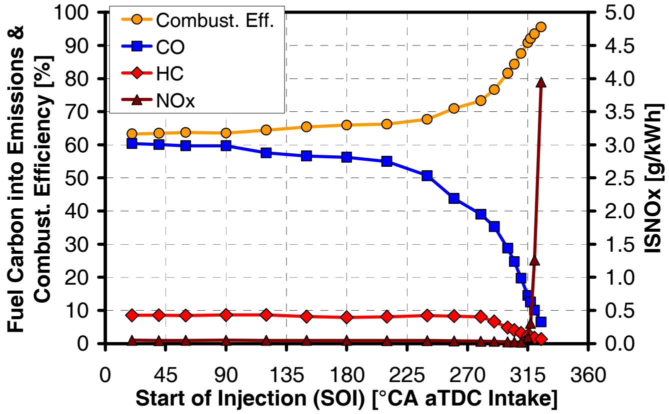

Figure 10. Combustion efficiency and emissions as a function of start of injection for the 8-hole injector. Low swirl (SR = 0.9) and P$_{inj}$ = 120 bar.

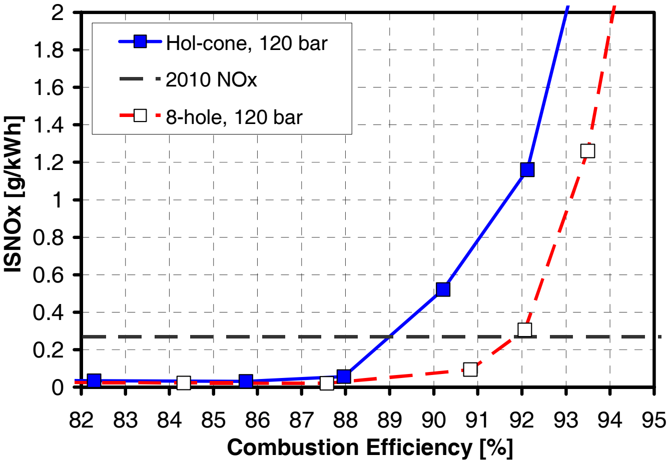

Figure 11. Effects of injector type on the combustion-efficiency/NO$_X$ tradeoff.

---

[8] It should be noted that the hollow-cone injector data was taken with only 5°CA resolution in SOI near the NO$_X$ limit. Had another data point been taken near the NO$_X$ limit, the hollow-cone injector base case might have had a combustion efficiency slightly higher than 89%, which would have brought it closer to the high-swirl line.

by 3% at the NO_X knee, from 88% for the hollow-cone base case to 91% for the 8-hole injector, and this same spread holds at the NO_X limit, where combustion efficiency is increased from 89% to 92%. This corresponds to an increase in the IMEPg from 103 kPa to 111 kPa. These findings are consistent with those of Steeper and De Zilwa [21] who found that an 8-hole injector significantly improved the combustion-efficiency/NO_X tradeoff, compared to a hollow-cone injector, in an automotive-size HCCI engine.

Figure 12 shows a comparison of the heat-release rates (HRR) for the 8-hole injector at the NO_X knee (SOI = 315°CA), the hollow-cone injector at the NO_X knee (SOI = 295°CA), and premixed fueling. The 8-hole injector has a higher peak HRR and shorter 10-90% burn duration compared to the hollow-cone injector. This indicates that the fuel burns more rapidly, and it is in agreement with the higher combustion efficiency observed at the NO_X knee. For the premixed case, which has a low combustion efficiency, the peak HRR is much lower and the burn duration much longer than either of the two fuel-stratified cases. Since CA50 was fixed at TDC, these changes in burn duration cause the start of combustion (represented by the 10% burn point) to occur latest for the 8-hole injector and earliest for the premixed case. The premixed case also has a long tail ensuing from the peak of the HRR because the late-combustion reactions (including $CO \rightarrow CO_2$ burnout) are very slow due to the low ϕ and the resulting low combustion temperatures. The HRR profiles for the stratified cases are more symmetric about TDC, and the ensuing tail is much shorter, because the $CO \rightarrow CO_2$ burnout is more rapid due to the locally higher ϕ. The tail for the 8-hole injector is slightly shorter than that of the hollow-cone injector, suggesting that there is less fuel at low-ϕ mixtures, in agreement with the improvement in the combustion-efficiency/NO_X tradeoff with this injector (noted in Fig. 11). The total amount of heat released, which is calculated from the integrated area under the HRR curve from 340° to 420°CA, is 332 J for the 8-hole injector, 316 J for the hollow-cone injector, and 230 J for the premixed case. This is an indication of the amount of fuel burned, and is proportional to the respective combustion efficiencies of 91%, 88%, and 64%.

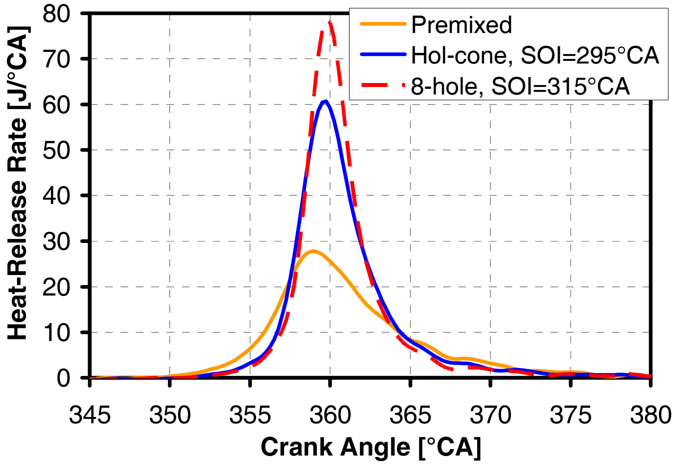

Figure 12. Comparison of heat-release rates for the 8-hole injector at the NO_X knee (SOI = 315°CA), the hollow-cone injector at the NO_X knee (SOI = 295°CA), and premixed fueling. ϕ = 0.12 for all cases.

Effects of Swirl – In contrast with the hollow-cone injector, increased swirl is slightly detrimental to the combustion-efficiency/NO_X tradeoff for the 8-hole injector. This is shown in Fig. 13, which presents all the 8-hole injector cases along with the hollow-cone data from Fig. 10. As can be seen for the 8-hole injector, the NO_X knees for the low- and high-swirl cases are virtually identical; however, beyond the knee, NO_X emissions rise more rapidly with high swirl so that at the NO_X limit, the combustion efficiency is about 0.5% worse than the low-swirl case. Despite this opposite effect of increased swirl on the combustion-efficiency/NO_X tradeoff for the two injectors (Fig. 13), high swirl slows the rate of fuel/air mixing for both injectors (Fig. 14). For the 8-hole injector, however, the SOI at the NO_X knee is only shifted about 5° earlier as compared to a 10° shift for the hollow-cone injector, as shown in Fig. 14.

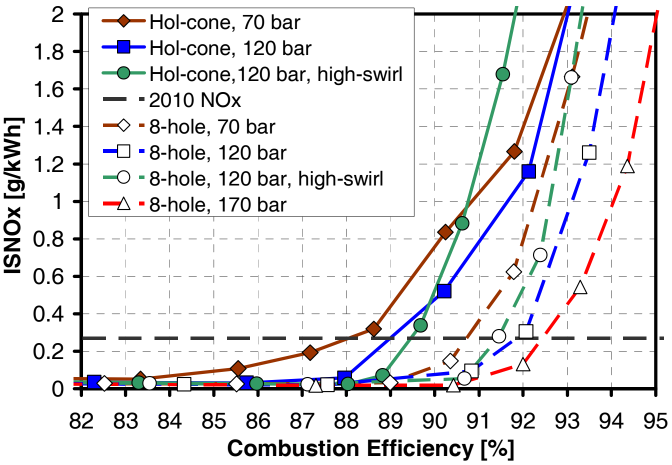

Figure 13. Combustion-efficiency/NO_X tradeoff for all cases.

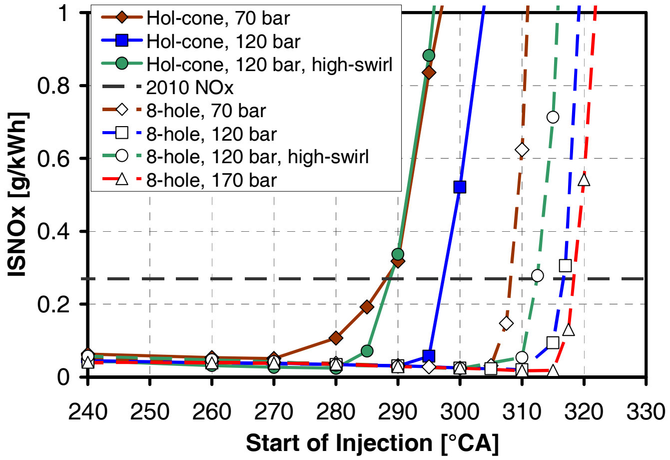

Figure 14. Rise in NO_X emissions with delayed injection timing.

Effects of Injection Pressure – Similar to the hollow-cone injector, reducing the injection pressure to 70 bar is detrimental to the performance of the 8-hole injector. The combustion efficiency at the NO_X knee is reduced by about 1%, compared to the 8-hole injector at P_{inj} = 120 bar, as shown in Fig. 13. Increasing P_{inj} to 170 bar has the opposite effect, improving the combustion efficiency 1% at the NO_X knee and about 0.5% at the NO_X limit. This high-injection pressure case with the 8-hole injector at low swirl showed the best performance of all the methods examined. Compared to the base case, it improved the combustion efficiency by 3.5% at the NO_X limit. Overall, this represents a very substantial improvement in combustion efficiency from 64% (without fuel stratification) to 92.5% at the NO_X limit.

These changes in injection pressure also affect the mixing rate as might be expected due to the change in the fuel-jet momentum. As evident in Fig. 14, the SOI for the rapid rise in NO_X emissions occurs about 7° earlier for P_{inj} = 70 bar and about 2.5° later for P_{inj} = 170 bar, compared to the P_{inj} = 120 bar case. (A similar shift can be observed also for the hollow-cone injector.)

CAUSE OF IMPROVEMENT IN THE COMBUSTION-EFFICIENCY/NO_X TRADEOFF

As discussed above, the combustion-efficiency/NO_X tradeoff and SOI vs. NO_X emissions are compared in Figs. 13 and 14 for all the cases investigated. Although Fig. 13 plots NO_X vs. combustion efficiency and Fig. 14 plots NO_X vs. SOI, there is a strong similarity between the two plots. In particular, the order and relative spacing of the curves is almost the same in both plots (with the one exception of the hollow-cone high-swirl case). This strong similarity indicates that for all but one of the methods examined, a later SOI at the NO_X limit results in a higher combustion efficiency. In other words, acceptable NO_X at a later SOI is obtained for techniques that provide faster fuel/air mixing that more quickly reduces the equivalence ratios of the richest regions below 0.6. Evidently, these fast-mixing conditions also produce fewer regions with $\phi < 0.2$ where combustion efficiency is low. We hypothesize that the reason for this beneficial effect is that with a later SOI there is less time for the in-cylinder flows and turbulence (*i.e.* mixing not produced by the injection process) to form overly lean regions by transporting fuel out of the main fuel pockets that are produced by the fuel-injection process. For the high-swirl cases, fuel/air mixing is no longer dominated by the fuel-injection process. Thus, this hypothesis no longer applies, which is consistent with the high-swirl exception noted above. Based on this hypothesis, additional changes to the fuel injectors and/or higher injection pressures that further increase the rate of the injector-driven fuel/air mixing could potentially improve the combustion-efficiency/NO_X tradeoff even more.[9]

FUEL-DISTRIBUTION MEASUREMENTS IN THE OPTICAL ENGINE

To better understand the reasons for the changes in the combustion-efficiency/NO_X tradeoff with the various fuel/air mixing techniques, chemiluminescence imaging and quantitative fuel-PLIF imaging were applied in the optically accessible engine. The same 8-hole injector was used in both engines, and the hollow-cone injector was the same as the one used in the metal engine except that it had a slightly different cone angle of 54° compared to 52° for the metal engine. As discussed previously, the optical engine has the same basic combustion chamber geometry as the metal engine. However, compared to the metal engine, which has a shallow bowl in the piston, the optical engine has a flat-top piston-crown window, a much larger ring-land crevice, and also spacer-ring windows (see Figs. 3 and 4). This causes the heat transfer at the piston top and cylinder wall to differ from that of the metal engine. Nevertheless, the mixing processes in the central region of the combustion chamber, away from the boundaries, should be similar to the metal engine. The difference in piston-top geometry between the two engines should not have a big effect, since the piston is at a low position at the injection times that were investigated. Even at a very late SOI of 315°CA, the distance from the cylinder head to the piston top for the optical engine is 30.3 mm, and for the metal engine it varies from 27.5 mm at the piston top to 38.7 mm at the bottom of the bowl. Thus, the average distance to the metal-engine piston is similar to that of the optical engine, and this distance is large compared to the depth of the bowl (11.2 mm). In addition, squish flows in the metal engine should not be strong due to the relatively narrow piston rim and large rim-to-head clearance. More importantly, these flows appear to have a minimal effect on the fuel distributions in the central region of the combustion chamber, since the measured distributions in the optical engine correlate well with emission measurements from the metal engine, as will be shown later. Finally, emission trends measured in the optical engine (not shown here) confirm that the overall bulk-gas combustion is similar. The only substantial difference is higher HC levels in the optical engine for premixed and early-DI operation, which are the result of incomplete combustion in the large crevice [27,28].

DIRECT INJECTION CHEMILUMINESCENCE IMAGES

The effects of fuel stratification on combustion were first examined using chemiluminescence imaging. Figure 15 shows chemiluminescence images of iso-octane combustion at ϕ = 0.12 obtained through the piston-crown window. The fuel was directly injected with a hollow-cone GDI injector in an 11/1 skip-fired mode. The temporal sequence of images in the top row (Fig. 15a) shows an early injection at SOI = 40°CA, and the bottom row (Fig. 15b) shows a late injection at SOI = 290°CA. CA50 was at 360°CA (TDC) for the early injection case, and 359°CA for the late injection case. For these particular experiments, a CR = 18 piston was installed and P_{in} = 100 kPa. The camera intensifier gain had to be ad-

---

[9] The 8-hole injector is capable of injection pressure up to 200 bar, which could potentially increase the NO_X-limited combustion efficiency even further.

(a) Early Injection (SOI = 40°CA)

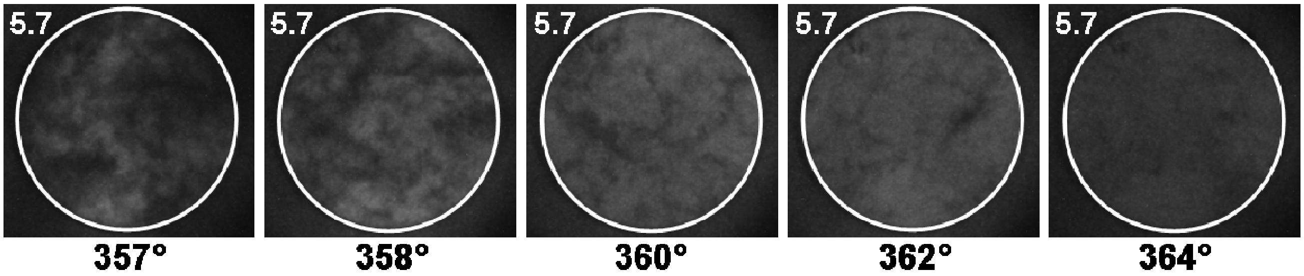

(b) Late Injection (SOI = 290°CA)

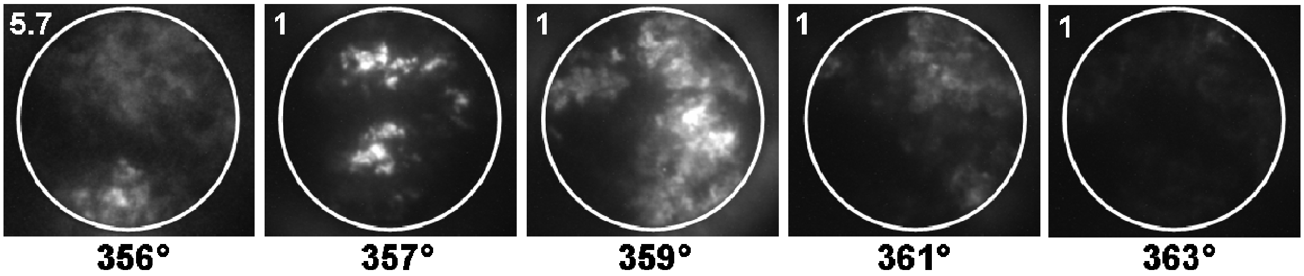

Figure 15. Chemiluminescence image sequences of iso-octane combustion at ϕ_{in} = 0.12, obtained through the piston-crown window. (a) Early fuel injection (SOI = 40°CA) from a hollow-cone GDI injector in 11/1 skip-fired mode. (b) Late injection (SOI = 290°CA). CA50 = 360°CA (TDC) for the early injection and CA50 = 359°CA for the late injection. CR = 18, P_{in} = 100 kPa, 1200 rpm. The white number in the upper left of each image shows the relative gain. Images shown are representative images at each crank angle.

justed according to the amount of light emission, and the relative gain factor is shown in the upper left corner of each image. To minimize blurring due to fluid motion, a 35 μs gate (1/4°CA at 1200 rpm) was used. The images shown have been selected as being representative of sets of twelve images taken at each crank angle.

Early Injection – As can be seen, the combustion is relatively homogeneous for the early injection case in Fig. 15 (a). However, inhomogeneities can be observed during the initial part of the combustion process, as evident in the 357°CA image. For SOI = 40°CA, fuel, air from the intake, and a small amount of residuals (consisting only of air due to the skipfired operation) are well mixed by the time of combustion [14]. Thus, the inhomogeneous appearance at 357°CA is the result of thermal non-uniformities and initial autoignition of the hotter regions. In a previous study, it was shown that this thermal stratification is mainly due to heat transfer and turbulent transport during compression [14]. By 358°CA, the inhomogeneities have begun to diminish as reactions start to occur in the cooler regions, but the chemiluminescence intensity does not change noticeably. This is probably due to the relatively long kinetic timescales for this low ϕ_{in} of 0.12. By the crank angle of peak heat-release rate at 360°CA, most regions are reacting, producing a relatively homogeneous chemiluminescence. Since chemiluminescence imaging is a line-of-sight technique, the emission from the reaction zones along the path length of 5.6 mm (clearance height at TDC for this CR = 18 piston) is integrated, which partially contributes to the homogeneous appearance. The luminosity is still very weak, even though 360°CA is the peak of the HRR, and has not changed much from 358°. This suggests that this early-injection case has a low combustion rate and low combustion temperatures, as might be expected for this dilute mixture. This is in agreement with the low combustion efficiency due to incomplete combustion for a SOI of 40°CA in Fig. 2. Beyond 360°CA, the chemiluminescence becomes more uniform, and the intensity remains fairly constant until 362°CA. This near-constant chemiluminescence intensity mostly likely occurs because at these dilute low-temperature conditions, the chemical-kinetic timescales for the combustion reactions are long, relative to the timescales associated with progressive autoignition from hotter to colder zones. By 364°CA, the intensity has started to uniformly diminish as the end of combustion approaches.

Late Injection – For the late injection case of SOI = 290°CA in Fig. 15b, the images show substantial inhomogeneity. At 356°CA (which is 3° before the peak of heat-release rate at 359°CA), the contrast between the bright and dark regions of the image is much greater than that for the early injection case in Fig. 15a. By 357°CA, the reacting zones appear much brighter, even with a gain that is nearly six times lower. This is because the late injection has produced a stratified fuel/air mixture, with the fuel being concentrated in localized regions where ϕ is well above ϕ_{in} = 0.12. These higher ϕ regions have faster reaction rates and higher combustion temperatures. There are many regions that are dark, either because there is no fuel, or the fuel/air mixture is too lean to show significant chemiluminescence at this crank angle. By the peak of combustion at 359°CA, more regions have ignited, and the image is significantly brighter overall. However, there are still relatively large regions with little or no chemiluminescence due to fuel stratification produced by late injection. The much stronger chemiluminescence emission, compared to the well-mixed case, is consistent with the higher combustion efficiency for late injection in the metal engine seen in Fig. 2. Past the peak in the heat-release rate at 359°CA, the chemiluminescence intensity decreases, and by 363°CA, most of the combustion is over.

Sources of Light Emission – The sources of this chemiluminescence have been examined using spectroscopic analysis [12,29], which showed that during the main hot combustion, the chemiluminescence is predominantly due to the CO continuum (*i.e.*, the continuous emission band resulting from the CO + O reaction). Recent high-resolution measurements by the authors, presented in [29], show that CH, CH_2O, HCO, and OH also contribute to the chemiluminescence, and that red and near infrared bands of H_2O and O_2 also emit strongly (probably due to thermal excitation, rather than chemiluminescence). Since the photocathode of the intensifier had low sensitivity in the red and infrared, and a glass lens was used (blocking ultraviolet light), the chemiluminescence images in Fig. 15 are dominated by emission from the CO continuum with some contributions from CH, CH_2O, and HCO. Since analysis shows that the CO + O reaction which creates the CO-continuum emission occurs at the same time as the main high-temperature heat-releasing reactions [29], the chemiluminescence images should also track these high-temperature combustion reactions.

Chemiluminescence images can provide a good qualitative picture of the effects of fuel stratification on the overall combustion process. However, they do not directly correspond to fuel distributions. Spatially-resolved two-dimensional fuel distributions can be measured using fuel-PLIF imaging. Accordingly, the various stratification techniques will be examined using fuel-PLIF imaging in the following sections.

COMPARISON OF HOLLOW-CONE AND 8-HOLE INJECTOR FUEL DISTRIBUTIONS USING PLIF

Fuel distributions from the hollow-cone and 8-hole injectors are examined first, since the 8-hole injector gives the most significant improvement in performance compared to the base-case hollow-cone injector. The hollow-cone injector used here had a cone angle of 54°, which was slightly different than the 52° cone angle used for the metal-engine data. The reason for this difference is that the 54° injector failed before all the metal-engine tests were complete, so the closest available substitute, the 52° injector, was used. However, before the failure, a test in the metal engine at the base condition showed that the emission trends for both injectors were very similar. The only differences were that the SOI for the onset of the rise in NO_X (see Fig. 14) was shifted about 5°CA later for the 54° injector, and with this shift, the combustion efficiency at the NO_X knee improved slightly from 88 to 88.5%.

PLIF images were obtained in an inert atmosphere of N_2, as discussed previously, to prevent quenching of the toluene fluorescence. The images were acquired at 365°CA for a series of SOIs for each test case. Near the NO_X knee they were acquired every 5° in SOI. The images were taken in sets of 20, mostly at a plane 4 mm from the firedeck, which is the mid-plane at TDC. Representative equivalence-ratio maps obtained from the fuel-PLIF imaging technique are presented. It should be noted that for these experiments, the CR = 14 piston was installed and P_{in} = 135 kPa, identical to the conditions used for the metal-engine data in Figs. 7 – 14.

Equivalence-Ratio Maps – The hollow-cone injector base-case ϕ-map sequence is first shown in Fig. 16. With SOI = 40°CA, the fuel is well mixed as can be seen by the uniform dark blue color. This color indicates a low ϕ (ϕ = 0.12 in this case) and corresponds to regions of poor combustion efficiency. With SOI = 240°CA, the fuel is still fairly well mixed, but is starting to show a small

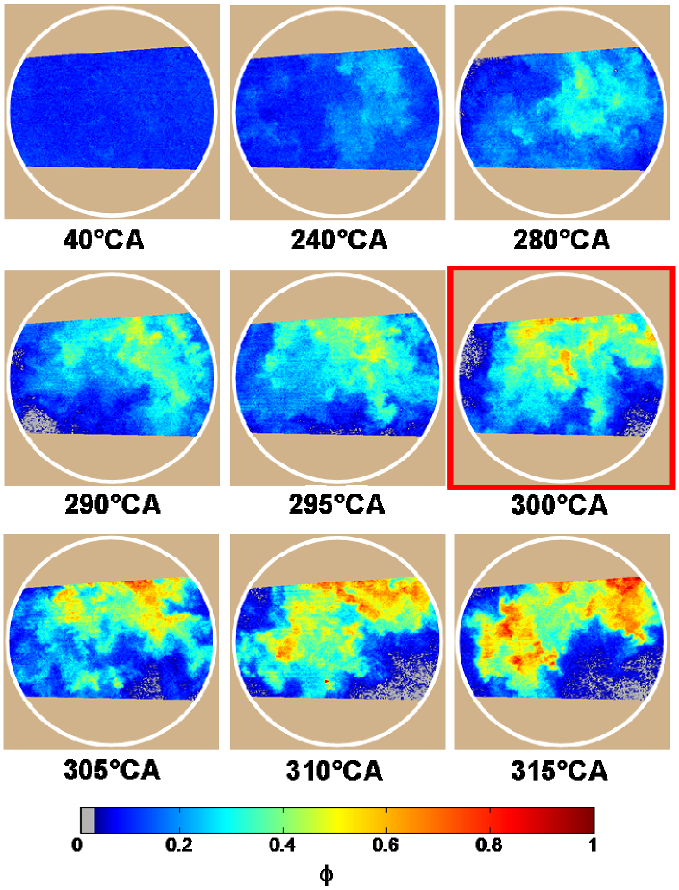

Figure 16. Equivalence-ratio maps at 365°CA for the hollow-cone injector base case for different SOI in the plane 4 mm below the firedeck. Operating conditions: P_{inj} = 120 bar; SR = 1.3; ϕ = 0.12; 1200 rpm; CR = 14; P_{in} = 135 kPa; intake temperatures were set to match those of the metal engine with CA50 = TDC. The white circle around each image shows the 70 mm diameter field of view through the piston-crown window. The red box indicates the NO_X knee.

amount of stratification. With an SOI 40° later (280°CA), the high-ϕ region in the upper right portion of the map has become much larger and more distinct, and the low-ϕ regions are reduced in area. Beyond 280°CA, the rate of stratification increases, and the interval in SOI between the displayed images is reduced. At the same time, the size of the rich region and the maximum ϕ both increase. Since the fueling rate was constant, other regions have to become leaner. Thus, $\phi \approx 0$ regions, represented by the gray color, start to appear at the outer boundaries of the map, and more near-zero ϕ regions where fuel has not yet been well distributed are probably present outside the field of view. The fuel is generally clustered near the center, as might be expected with a late injection timing, since the in-cylinder turbulence and the flows produced by the fuel injection do not have enough time to uniformly distribute the fuel. Also, as the fuel becomes more stratified, the fuel distribution appears to develop sharper boundaries between the fuel-rich and fuel-lean regions. The SOI = 300°CA case, which corresponds to the NO_X knee, has a few fuel-rich regions with a maximum ϕ in the 0.6 – 0.7 range. As the SOI is delayed beyond the NO_X knee, the non-zero low-ϕ regions generally decrease in size, which is consistent with the improvement in combustion efficiency observed in the metal engine. However, beyond the knee, the portion of the high-ϕ regions with $\phi > 0.6$ increases substantially, and the maximum ϕ rises well above 0.7, explaining the rapid rise in NO_X observed in the metal-engine data. Overall, the trends in the ϕ maps in Fig. 16 agree well with the metal-engine data in Fig. 7a.

Figures 17a and 17b show a direct comparison between the ϕ-map sequence in Fig. 16 for the hollow-cone injector base case and the corresponding image sequence for the 8-hole injector at the same low-swirl and P_{inj} = 120 bar operating condition. In agreement with the metal-engine data in Figs. 7a and 10, these image sequences show a delayed onset of stratification with the 8-hole injector. For the earliest SOI shown in Fig. 17 (290°CA), the 8-hole injector shows only a small amount of stratification, while stratification for the hollow-cone injector is already significant, as discussed above. For each subsequent SOI, the hollow-cone injector ϕ maps show more stratification with more high-ϕ regions in the center and more low-ϕ regions towards the periphery. Thus, the 8-hole injector has a higher fuel/air-mixing rate compared to the hollow-cone injector. This is in agreement with the metal-engine NO_X emissions starting to rise at a later SOI for the 8-hole injector, as Fig. 14 shows.

To better compare the fuel distributions near the onset of NO_X production, the ϕ maps for the hollow-cone injector are shifted so that the SOI that corresponds to the NO_X knee is aligned with that of the 8-hole injector. From Figs. 17b and 17c, it can be seen that the ϕ maps look quite similar for both injectors when the NO_X knees are aligned. This is perhaps surprising, considering the fact that the injectors have very different spray patterns, as visualized by Steeper and De Zilwa [21]. The maximum equivalence ratios are similar for each aligned ϕ map, and this is in agreement with Fig. 14, which shows similar rates of increasing NO_X for SOI beyond the NO_X knee. On the other hand, the NO_X knee is at 315°CA for the 8-hole injector, so 15°CA less time is needed for the 8-hole injector to achieve the same level of mixing.

Several observations can be made regarding the structure of the fuel stratification. The fuel distributions do not show any resemblance to the original spray patterns emanating from either injector. Specifically, the ϕ maps for the hollow-cone injector do not show any "hollow" toroidal appearance, and those for the 8-hole injector do not display any identifiable jet-like structures or even any intermittent pattern as might be expected for a mixture produced by eight separate jets. This observation holds even for the latest SOI = 325°CA, which is only 40°CA before the images were acquired. For the hollow-cone injector a single fuel-rich region is perhaps not unexpected, since injection into a high-density ambient can cause the hollow cone to collapse and appear more like a filled cone [26]. However, the similar fuel pattern for the 8-hole injector was unexpected. This pattern indicates that the 8-hole injector produces very high mixing rates. One explanation for this is that the air-entrainment rates into the individual fuel jets are sufficiently high that each jet expands and merges with the adjacent jets.[10] The consolidation of the fuel into a single fuel-rich region is also probably partly due to the relatively narrow (70°) included angle of the sprays. With this narrow angle, the jets do not spread rapidly from one another, and a low-pressure region might develop in the center of the cone produced by the eight jets, which would help draw the vaporized fuel towards the center. Finally, in-cylinder turbulence will also provide mixing.

This similarity between the fuel distributions produced by the hollow-cone and 8-hole injectors is not consistent with the findings of Steeper and De Zilwa [21], who also compared hollow-cone and 8-hole injectors. Using PLIF imaging, they observed that the hollow-cone injector produced fairly consolidated fuel packets, and the 8-hole injector distributed the fuel more widely in smaller and more numerous fuel packets. There appear to be at least three reasons why the observations in Ref. [21] are different from those in the current study. First, there was considerably more mixing time in the current study, since the images were acquired at 365°CA, as compared to 330°CA in Ref. [21]. Since the SOIs were similar for the two studies, there was twice as much time for mixing in the current study. (The engine speed was 1200 rpm for both studies.) Second, the images in the current study

---

[10] Spray visualization images reported by Steeper and DeZilwa [21] showed distinctive jets emanating from their 8-hole injector. The Mie scattering from the liquid jets could be seen even 15°CA after the SOI. However, for our experiments, the jets were most likely vaporized much more rapidly during the injection process. This is due to the higher in-cylinder temperatures caused by the higher intake temperature and higher compression ratio. The fast vaporization of liquid droplets may also help increase the air entrainment and mixing rate of the fuel jets.

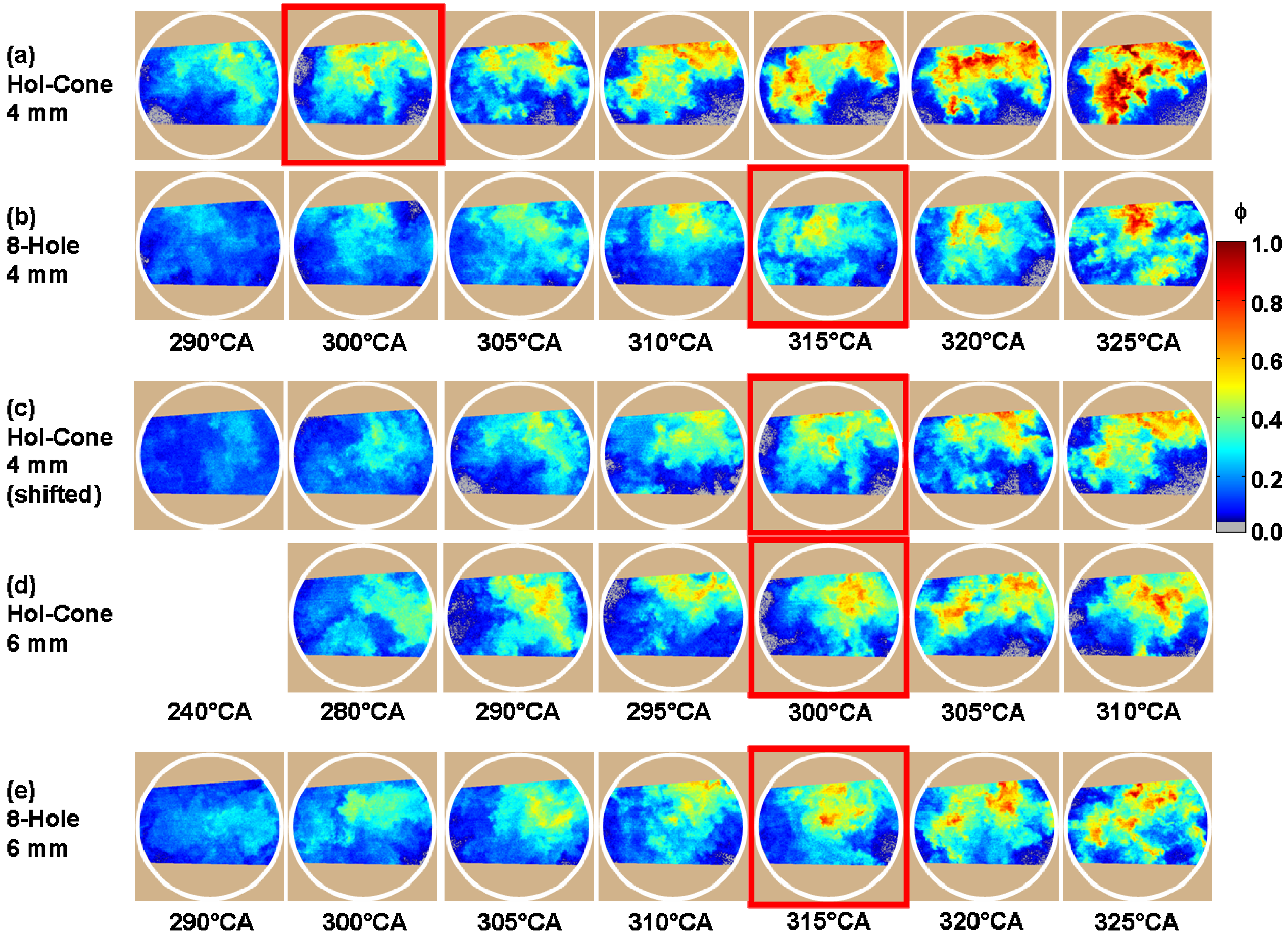

Figure 17. Equivalence-ratio maps for the hollow-cone and 8-hole injectors at different SOI and different elevations. From top to bottom: (a) hollow-cone injector base case at mid-plane, 4 mm below the firedeck, (b) 8-hole injector at mid-plane, (c) hollow-cone injector base-case sequence shifted to align NO_X knee with 8-hole injector, (d) hollow-cone injector base case at lower elevation, 6 mm below the firedeck, (e) 8-hole injector at lower elevation. The red boxes indicate the respective NO_X knees for each case. Operating conditions: P_{inj} = 120 bar; SR = 1.3; ϕ = 0.12; 1200 rpm; CR = 14; P_{in} = 135 kPa; intake temperatures were set to match those of the metal engine with CA50 = TDC.

were taken in the mid-plane of a pancake combustion chamber near TDC, when the fuel is compressed into a small volume. On the other hand, the engine in Ref. [21] had a pent-roof configuration, and images were taken 4 mm above the piston at 30°CA before TDC. Thus, the fuel was more widely distributed, and the laser sheet was proportionally lower in the charge volume for the images in Ref. [21]. Third, in-cylinder flows and turbulence characteristics are likely different between these two engines.

Statistical Evaluation of Fuel Distributions – The equivalence-ratio maps provide an overview of the fuel distributions. However, it is difficult to compare exact values of ϕ and explain the 2.5% difference in combustion efficiency. (Note that this difference is 3% for the data in Figs. 11 and 13, which were acquired with the 52° cone-angle injector, as noted previously). A statistical evaluation of the fuel distribution can be provided by an equivalence-ratio probability density function (PDF). Furthermore, instead of just using one representative image, a more accurate ϕ PDF can be obtained by using all 20 images acquired at each condition. For both injectors, statistical analyses will be presented to provide quantitative data about the onset of regions that are sufficiently rich to cause NO_X formation, and to help investigate why the 2.5% higher combustion efficiency is observed for the 8-hole injector.

Figure 18 shows the ϕ PDFs for the hollow-cone injector base case. Each of the area-based PDFs in Fig. 18a are obtained by first calculating the fraction of the total imaged area associated with each ϕ value to obtain an individual PDF for each image in the image set, and then averaging across the image set. The PDF for the early SOI = 40° case is tall and has a narrow peak, indicating the charge is well-mixed. As the SOI is delayed, the ϕ distribution becomes wider and flatter, thus extending to higher ϕ. This shows that more fuel-rich regions are being produced with the stratification. The near-zero ϕ regions also become larger in area with stratification, and the non-zero low-ϕ regions become smaller. This leads to a bimodal distribution of ϕ, with a small peak near ϕ = 0.04 and a second peak at higher ϕ values. This bimodal appearance is detectable in the SOI = 300°CA curve in Fig. 18a, and becomes more distinctive beyond the NO_X knee in the 315°CA curve. In Figs. 17a and 17c this coincides with the increase in gray and red regions in the ϕ maps for delayed SOI.

Since the combustion efficiency is a function of the amount of fuel mass burned, fuel-mass-weighted PDFs are more relevant than the area-based PDFs for understanding engine performance, and for predicting CO and NO_X emissions [19,20]. Mass-weighted PDFs are calculated by multiplying the area-based PDF value of each bin with the ϕ of that bin. Therefore, the mass-based PDFs of Fig. 18b represent the relative fuel mass associated with each ϕ. As can be seen by a comparison of the stratified cases in Fig. 18b with those in Fig. 18a, the ϕ weighting of the mass-based PDFs increases the values at high ϕ and reduces the values at low ϕ compared to the area-based PDFs.

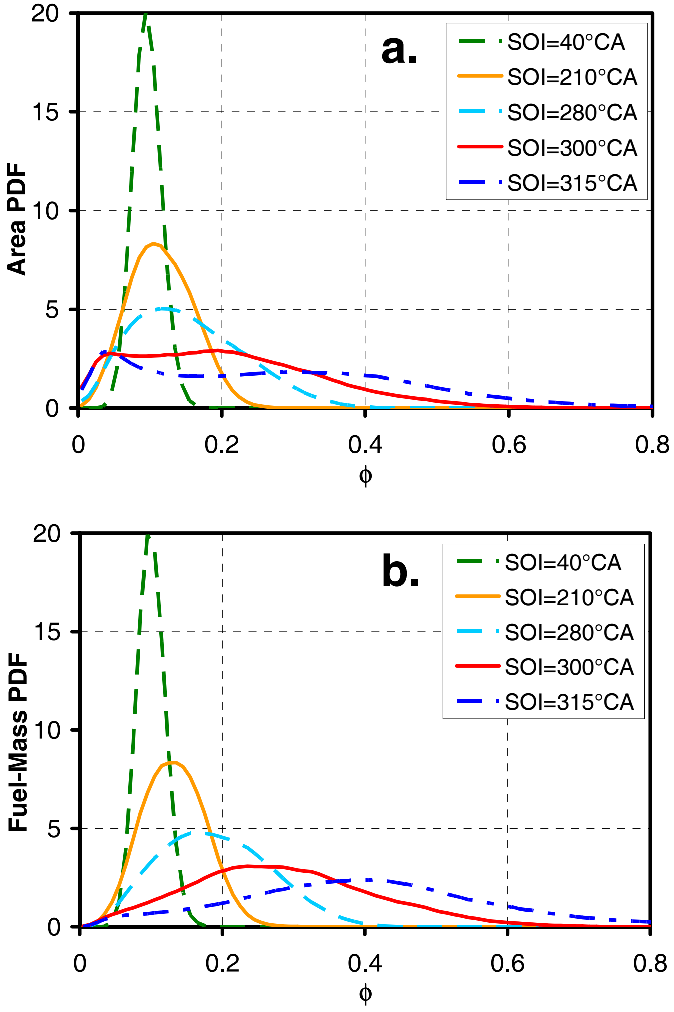

Figure 18. (a) Area-based and (b) mass-based PDFs of equivalence ratio for the hollow-cone injector base case at various SOI.

Since the area under the mass-based PDF is normalized to unity, it is impossible to compare the amount of fuel present in the images for both injectors. Therefore, fuel-mass-weighted histograms will be used as the basis of comparison. This allows the relative fuel mass at each condition to be obtained by integrating the mass histogram. However, it should be noted that not all of the fuel will be captured in the images due to the limited field of view.

The mass-weighted ϕ histograms for the hollow-cone injector base case are shown in Fig. 19. The overall trends are very similar to those of the mass-based PDFs. However, the mass histograms do not decrease in height with SOI as much as the mass PDFs do, since the areas under the curves are not being normalized to 1. The areas under the mass histograms are actually increasing, indicating that the amount of fuel imaged is increasing with delayed SOI. In other words, more fuel remains in the field of view. The overall amount of fuel in lean re-

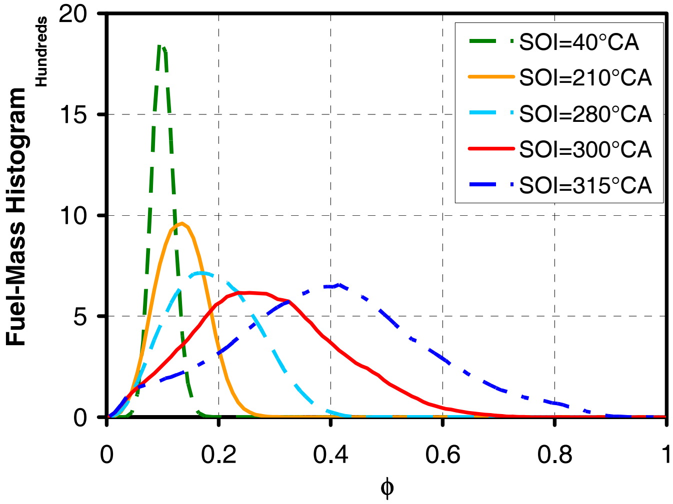

Figure 19. Mass-weighted histograms of equivalence ratio for the hollow-cone injector base case at various SOI. 4 mm plane.

gions with ϕ below about 0.14 [11] (obtained by integrating the curves up to that point) progressively decreases with delayed SOI. This correlates with improved combustion efficiency, due to the higher ϕ (Fig. 1) for delayed SOI (Fig. 7a). The amount of fuel in regions with ϕ higher than about 0.6 remains low (corresponding to low NO_X levels) until after the NO_X knee at SOI = 300°. For SOI = 305°CA (not shown in Fig. 19), the histogram becomes substantially elevated for ϕ = 0.6, in agreement with the onset of significant NO_X in the metal engine. By SOI = 315°CA, the metal-engine data show a large amount of NO_X is being formed, which is consistent with the relatively large histogram values for ϕ in the 0.6 – 0.8 range. Thus, the improved combustion-efficiency/NO_X tradeoff with delayed SOI is well explained by the fuel-mass histograms.

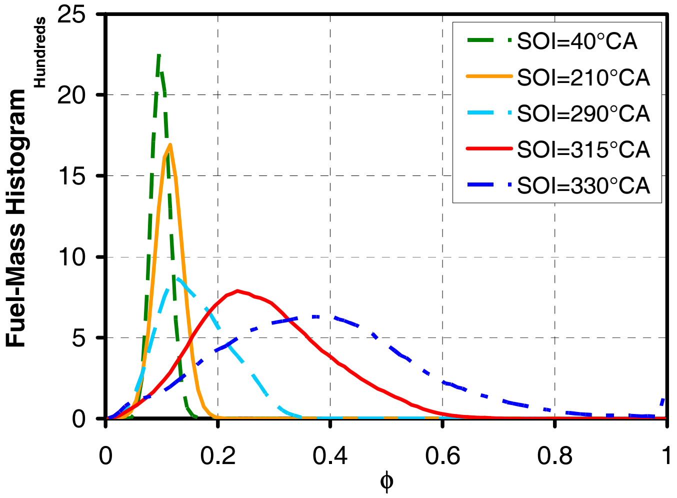

Figure 20. Mass-weighted histograms of equivalence ratio for the 8-hole injector (SR = 1.3, P_{inj} = 120 bar) at various SOI. 4 mm plane.

Figure 20 shows the mass histograms for the 8-hole injector. (Note that the scaling of the graph is different than that in Fig. 19.) It can be seen that the trends with SOI are similar to those of the hollow-cone injector, except that the latest SOI with an insignificant amount of fuel at ϕ > 0.6 shifts to 315°CA, in agreement with the shift in the NO_X knee shown in Fig. 14. As with the hollow-cone injector, the improvements in combustion-efficiency are explained by the reduction in the amount of fuel in the low-ϕ regions with delayed SOI. Beyond the NO_X knee, large regions with ϕ > 0.6, corresponding to high NO_X production, can be observed for SOI = 320°CA (not shown here) and SOI = 330°CA. Another significant difference compared to the hollow-cone injector is that the SOI = 210°CA mass histogram has nearly the same area under the curve for ϕ below about 0.14 as the SOI = 40°CA histogram. This is in agreement with Fig. 10, which indicates that changes in the combustion efficiency are not observed until after SOI = 210°CA with the 8-hole injector. It is also noteworthy that more fuel remains in the field of view with delayed SOI, similar to the hollow-cone injector.

To better compare the two injectors, mass histograms for the SOI at their respective NO_X knees are shown in Fig. 21 for two different elevations below the firedeck. The base elevation of 4 mm (which has been used for all previous histograms) is described first. The high-ϕ regions of the histograms for the two injectors nearly overlap, in agreement with the similar NO_X levels at the respective NO_X knees in the metal engine. However, the 8-hole injector has more fuel still within the field of view,

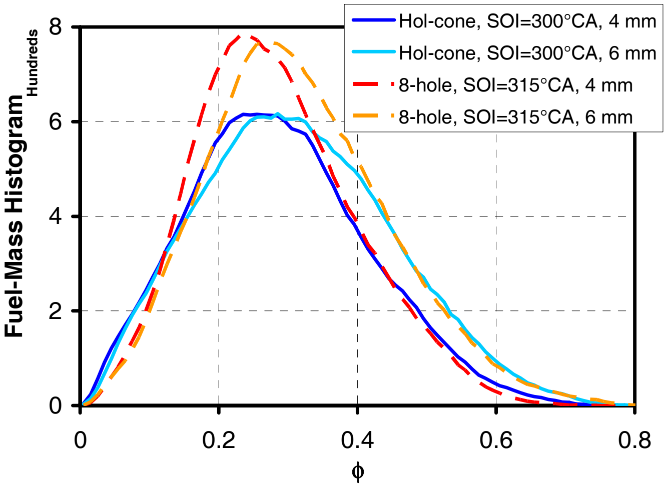

Figure 21. Mass-weighted histograms of equivalence ratio for the hollow-cone and 8-hole injectors for the SOI at the NO_X knee. Two elevations are shown; the base elevation at 4 mm below the firedeck (mid-plane at TDC), and 6 mm below the firedeck. SR = 1.3; P_{inj} = 120 bar.

---

[11] Although ϕ > 0.2 is required for complete combustion (see Fig. 1), the combustion efficiency decreases progressively as ϕ is reduced further. Thus, the very low ϕ regions are the primary contributors to the overall combustion inefficiency, while those closer to ϕ = 0.2 contribute significantly less. To reflect the greater importance of these low-ϕ regions, we have selected the critical ϕ for this discussion to be 0.14, which corresponds to a combustion efficiency of about 70%.

as can be seen by the larger area under the mass histogram. Moreover, the 8-hole injector has smaller histogram values below about $\phi = 0.14$ compared to the hollow-cone injector, which is in agreement with the higher measured combustion efficiency for the 8-hole injector. However, the difference in fuel amount below $\phi = 0.14$ is not large enough to fully explain the 2.5% difference in combustion efficiency observed in the metal engine. Examination of the ϕ maps at the NO_X-knee in Figs. 17b and 17c suggests that this may be due to the limited field of view of the images. For both injectors, it can be seen that most of the periphery of the main fuel pocket, where the $\phi < 0.14$ regions are located, is not visible in the images presented. Although the amount of fuel-pocket periphery captured varies from image to image, all images showed only a small portion of this boundary region. Therefore, a larger field of view is needed to fully explain the reason for the difference in the combustion-efficiency at the NO_X limit for the two injectors.

Lower Elevation – In order to investigate whether there was any vertical stratification of the fuel distribution, measurements were also made at a lower elevation for both injectors. These fuel distributions are shown in Figs. 17d and 17e. They were obtained at a plane 6 mm below the cylinder head, which was half way between the mid-plane and piston top at TDC. Compared to the 4 mm mid-plane ϕ maps in Figs. 17c and 17b, the overall trends are similar with a large fuel pocket near the center of the field of view. However, the lower elevation does show a slightly higher fuel concentration. Figure 21 shows that the fuel-mass histograms at the NO_X knee for this lower elevation are quite similar to those at the mid-plane for $\phi < 0.14$. However, the peaks of the histograms and the rich tails are shifted to higher ϕ, confirming that the fuel distribution is richer at the lower elevation. The amount of fuel with $\phi > 0.6$ increases for both injectors. This suggests that more NO_X forms in the lower part of the combustion chamber. Yet the metal-engine data indicate that the NO_X emissions still remain below the U.S. 2010 limit.

EFFECTS OF SWIRL ON FUEL DISTRIBUTIONS

Hollow-Cone Injector – The high-swirl ϕ maps for the hollow-cone injector are depicted in Fig. 22b. Compared to the base case in Fig. 22a, which is a reproduction of Fig. 17c, the high-swirl fuel distributions are substantially leaner at the NO_X knee and for SOIs near the respective NO_X knees. In addition, as the SOI is delayed from 280°CA to the NO_X knee at 290°CA, the fuel distribution shows almost no change, as also evidenced in the mass histograms in Fig. 23. This is in contrast to the base case in Fig. 22a, which shows a clear increase in stratification as SOI is delayed through the NO_X knee. By themselves, these leaner mixtures and lack of change with SOI could suggest that the swirl is mixing the fuel faster. However, the metal-engine results show that swirl produces a slower mixing rate (see Fig. 14). The data beyond the NO_X knee also show an apparent inconsistency between the image-derived and metal-engine results. For SOI = 310° (20°CA past the NO_X knee), the ϕ map in Fig. 22b and mass histogram in Fig. 23 show that there are not many regions with $\phi > 0.6$ in the field of view, while the metal-engine results in Fig. 14 indicate that this SOI produces very high amounts of NO_X. Accordingly, it can be postulated that there must be substantial regions with a higher ϕ that are not in the field of view. The fuel could be beneath the imaged plane, but there is no obvious reason why swirl would cause this. It is more likely that the swirl would affect the radial distribution of the fuel. Richer mixtures are cooler due to fuel vaporization cooling and reduced compression heating from the lower γ. Thus, these mixtures are more dense, and the centrifugal forces caused by the swirl would propel them radially outwards, explaining the paucity of fuel in the central region. After forming this radially stratified mixture, the centrifugal forces would continue to hinder the transport of fuel from the more-circumferential regions into the leaner central regions, explaining the slower mixing rates with swirl observed in the metal engine. It should be noted, however, that even with the slower mixing rate, swirl slightly increased the combustion efficiency compared to the base case at the NO_X knee for the hollow-cone injector (see Fig. 9).

8-Hole Injector – The effects of swirl on the 8-hole injector are overall similar to the hollow-cone injector, with the ϕ remaining low in the central region of the combustion chamber, as can be seen in Fig. 22d. However, for the 8-hole injector, increasing the swirl reduces the ϕ in the central region even more than it did for the hollow-cone injector. This can be seen by comparing the change for the 8-hole injector from Fig. 22c (low swirl) to Fig. 22d (high swirl) with the change for the hollow-cone from Fig. 22a (low swirl) to Fig. 22b (high swirl). This indicates that for the 8-hole injector, swirl causes a greater fraction of fuel to be located beyond the field of view compared to the hollow-cone injector high-swirl case. An explanation for this is that the fuel is injected with a spray angle 16° wider than that of the hollow-cone spray, so the outward momentum of the fuel is greater, especially if the hollow-cone spray collapses. In addition, the spray velocity is likely higher since the fuel is concentrated in 8 jets rather than being distributed uniformly around the cone. These effects, combined with swirl, appear to drive more of the fuel outward beyond the field of view for the 8-hole injector. This greater effect of swirl is perhaps related to the metal-engine results showing that high swirl slightly decreased the combustion efficiency at the NO_X limit for the 8-hole injector, in contrast to the slight improvement with high swirl observed for the hollow-cone injector (see Fig. 13).

The mass histograms in Fig. 24 show little change for a wide range of SOI, from 240°CA to 310°CA (NO_X knee), with the peak value remaining at $\phi = 0.13$. This crank-angle range is even wider than that observed for the hollow-cone injector (Fig. 23), providing further evidence of the large effect of high swirl on the fuel distribution with the 8-hole injector. As the SOI is delayed, the peaks are reduced in height but stay in the same position, and only

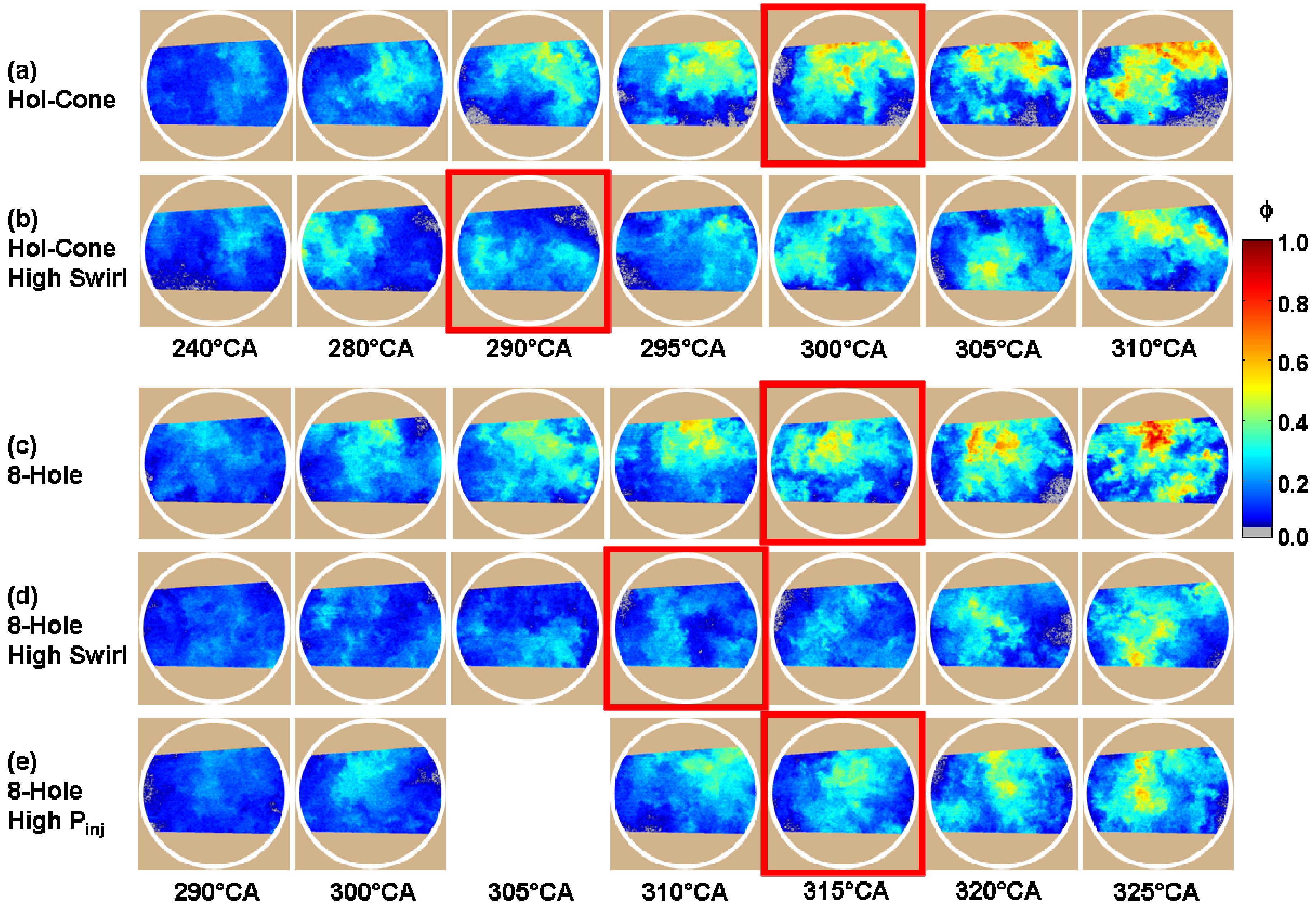

Figure 22. Equivalence-ratio maps for various test cases at different SOI. From top to bottom: (a) hollow-cone injector base case at SR = 1.3 and P_{inj} = 120 bar, (b) hollow-cone injector at high swirl (SR = 3.6) and P_{inj} = 120 bar, (c) 8-hole injector at SR = 1.3 and P_{inj} = 120 bar, (d) 8-hole injector at high swirl (SR = 3.6) and P_{inj} = 120 bar, (e) 8-hole injector at SR = 1.3 and high P_{inj} = 170 bar. The red boxes indicate the respective NO_X knees for each case. Operating conditions: ϕ = 0.12; 1200 rpm; CR = 14; P_{in} = 135 kPa; intake temperatures were set to match those of the metal engine with CA50 = TDC.

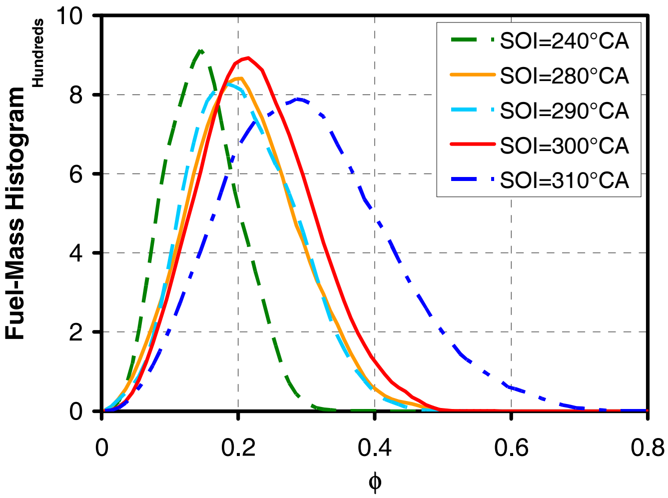

Figure 23. Mass-weighted histograms of equivalence ratio for the hollow-cone injector high-swirl case (SR = 3.6) at various SOI.

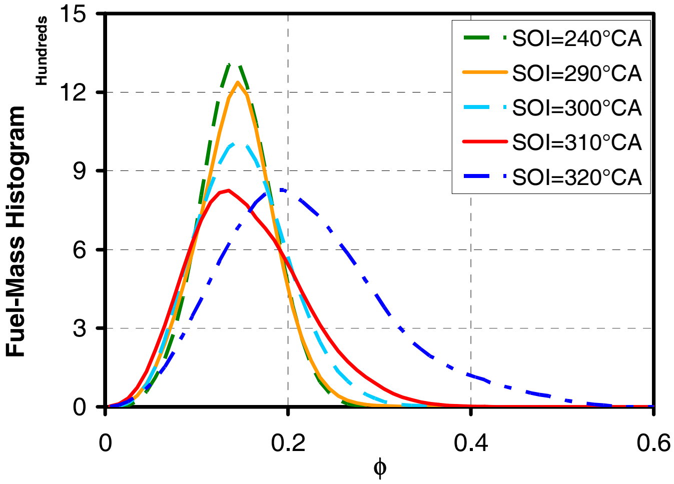

Figure 24. Mass-weighted histograms of equivalence ratio for the 8-hole injector with high swirl (SR = 3.6) at various SOI.

the tails extend to slightly higher ϕ. The areas of the mass histograms do not increase as expected with delayed SOI. Instead, they are nearly identical within this SOI range. This indicates that even for later injections up to 310°CA, swirl is causing the same amount of fuel to be located outside the field of view. This can be inferred from the ϕ maps in Fig. 22d as well. Starting with SOI = 320°CA, which is 10°CA later than the NO_X knee, the histogram shifts to higher ϕ. However, the maximum ϕ is still only about 0.5, suggesting that little if any NO_X is being produced by fuel within the field of view. Since the metal-engine results indicate that a significant amount of NO_X is produced at this SOI, there must be a substantial amount of stratified fuel-rich regions in the outer boundaries beyond the field of view, in agreement with the discussion in the previous paragraph.

EFFECTS OF INJECTION PRESSURE ON FUEL DISTRIBUTIONS

Hollow-Cone Injector – Figure 25 presents a comparison of equivalence-ratio maps obtained for the hollow-cone injector at low injection pressure and the base case at the same SOI. Only the most interesting SOIs are shown. As can be seen, with the lower P_{inj}, the mixture is already quite stratified at 240°CA compared to the base case. The mass histogram in Fig. 26 shows this as well. The SOI = 240°CA curve is similar in shape to the base-case curve in Fig. 19 for SOI = 280°CA, which is

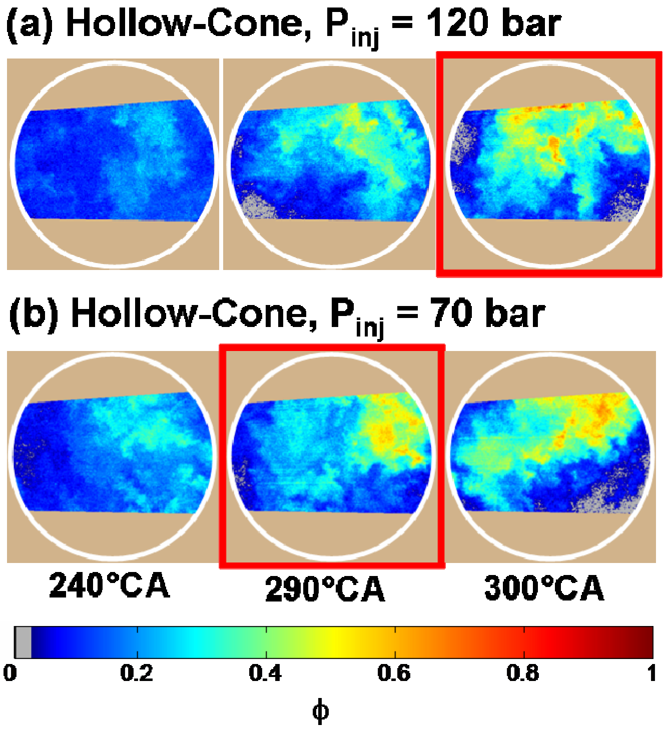

Figure 25. Equivalence-ratio maps at different SOI for the hollow-cone injector at (a) P_{inj} = 120 bar and (b) P_{inj} = 70 bar. The red boxes indicate the respective NO_X knees for each case.

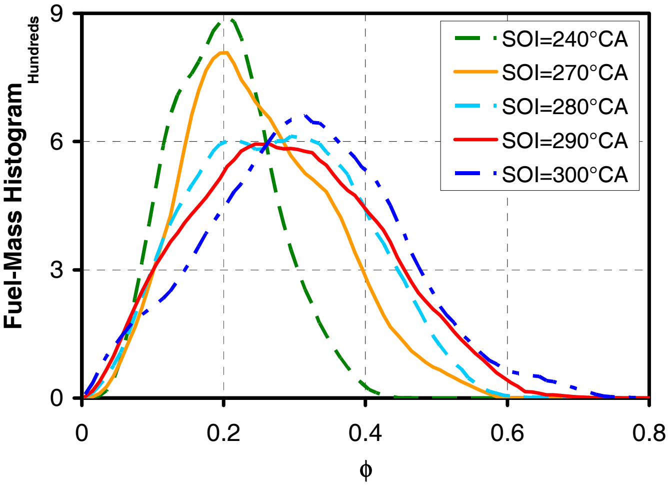

Figure 26. Mass-weighted histograms of equivalence ratio for the hollow-cone injector at low injection pressure (P_{inj} = 70 bar) for various SOI.

40°CA later in SOI. The maximum ϕ is slightly higher than 0.4 for both curves. However, the peak of the histogram is at a slightly higher ϕ of 0.2 for the P_{inj} = 70 bar, SOI = 240°CA curve. In agreement, the ϕ maps in Fig. 25 indicate that the P_{inj} = 70 bar case is more stratified than the base case for both SOI = 290°CA (NO_X knee) and SOI = 300°CA. The mass histograms also show that more fuel is in the imaged domain for SOI = 270 – 300°CA compared to the base case. These results indicate that the fuel is not penetrating outwards as much at this low injection pressure and these late injection timings. This corresponds to lower mixing rates compared to the base case, as shown with the earlier rise of NO_X emissions in Fig. 14.

8-Hole Injector – Two different injection pressures, 70 and 170 bar, were evaluated for the 8-hole injector and compared with the 120 bar case. Similar to the hollow-cone injector, the lower P_{inj} = 70 bar case has a lower mixing rate (see Fig. 14) than the 120 bar case. However, the ϕ maps in Fig. 27 do not capture this effect well. The ϕ maps appear similar for each SOI, and the P_{inj} = 70 bar case has a smaller fuel-rich region at the NO_X knee (outlined by the red box).

For the higher P_{inj} = 170 bar case, Fig. 22e shows that there is less fuel in the field of view for each SOI compared to the P_{inj} = 120 bar case in Fig. 22c. This is probably due to the fuel jets penetrating outwards faster with the higher P_{inj}. Since the jets were aimed downward as well as outward (Fig. 5), the high-ϕ regions could also have been below the imaging plane, as has been discussed. Thus, within the field of view, no overly rich regions were observed at the NO_X knee, similar to the high-swirl condition. The higher spray momentum enhances the mixing rate, so NO_X is lower for a given SOI (see Fig. 14).

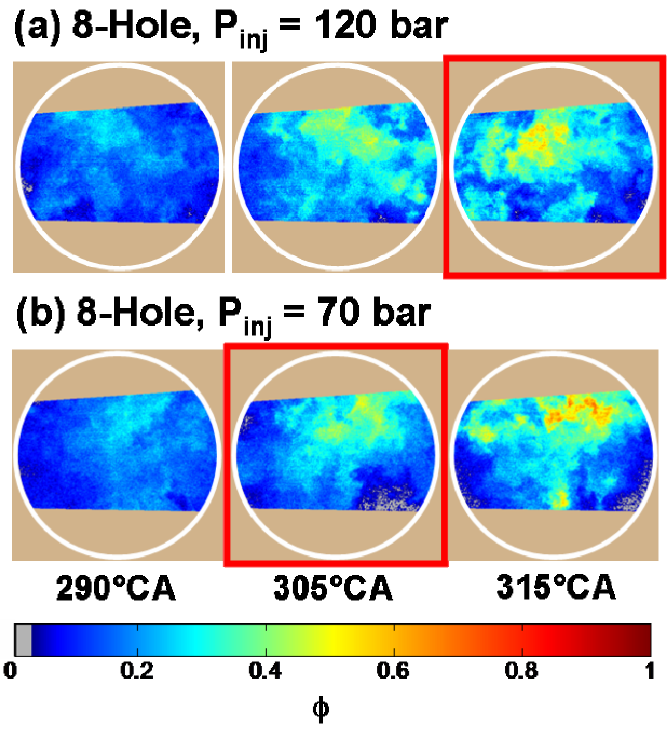

Figure 27. Equivalence-ratio maps at different SOI for the 8-hole injector at (a) P_{inj} = 120 bar and (b) P_{inj} = 70 bar. The red boxes indicate the respective NO_X knees for each case.

SUMMARY AND CONCLUSIONS

Combustion efficiency can be substantially improved for low-load HCCI combustion using fuel stratification. This can be achieved by delaying the fuel injection timing using a GDI injector. However, NO_X emissions start to rise very rapidly after a certain point, as the richest regions in the stratified fuel charge begin to exceed ϕ = 0.6. Thus, there is a tradeoff between combustion efficiency and NO_X. Several stratification techniques, such as different GDI injectors, swirl, and injection pressures have been examined to investigate which parameters are effective for improving the combustion-efficiency/NO_X tradeoff. Performance and exhaust emission measurements were obtained in an all-metal engine. Corresponding fuel distribution measurements were made with fuel PLIF in a matching optical engine. The PLIF images were reduced to equivalence-ratio maps using a novel technique to correct the signal for variation in temperature created by the fuel stratification. Spatial ϕ maps were used to visualize the fuel distribution, and fuel-mass histograms were used to statistically evaluate the distributions. The fuel used for this study was iso-octane, which is a good surrogate for gasoline. For all cases examined, the phasing was controlled so that CA50 was maintained at TDC as the fuel was stratified.

The main conclusions of this study follow:

1. Low-load combustion efficiency was improved substantially, from 64% to 89%, using delayed start of injection (SOI) from a swirl-stabilized hollow-cone injector at an injection pressure of 120 bar, before the NO_X emissions exceeded the U.S. 2010 limit. This condition was selected as the base case for comparison.
2. The 8-hole injector provided the single largest improvement in the combustion-efficiency/NO_X tradeoff over the hollow-cone injector. This injector allowed the combustion efficiency to be increased by 3%, from 89% to 92%, at the NO_X limit.
3. The fuel PLIF images agreed well with the metal-engine data for both injectors, as regions with ϕ > 0.6 started to appear with the onset of NO_X emissions. The delayed onset of stratification for the 8-hole injector was clearly observed in the ϕ maps.
4. The 8-hole injector produced a single large rich region near the center of the cylinder for fuel-stratified operation with a delayed SOI near the NO_X limit. It did not display small fragmented fuel pockets at the time of combustion, as might have been expected with 8 individual fuel jets.
5. For ϕ maps acquired at SOI with similar NO_X levels, the fuel distributions with the two injectors were

nearly the same, in agreement with the self-similar SOI vs. NO_X curves from the metal engine.

6. Detailed image analysis with fuel-mass histograms showed a strong correlation between the amount of fuel in rich ($\phi > 0.6$) regions and NO_X production. The increase in combustion efficiency was also correlated with the reduced amount of fuel in low-ϕ regions, but this finding was not conclusive since much of the periphery of the main fuel pocket was beyond the field of view.
7. Images acquired at 6 mm below the firedeck (halfway between the mid-plane and piston top at TDC) showed similar trends with SOI compared to those in the 4 mm mid-plane, indicating the validity of measurement trends in the mid-plane. However, the images at the lower elevation consistently showed a slightly higher ϕ than the mid-plane, showing that the fuel distribution was somewhat vertically stratified.
8. High swirl (SR = 3.2) slowed the mixing rate for both injectors, and it reduced the combustion efficiency for the 8-hole injector by 0.5% at the NO_X limit. However, high swirl improved the combustion efficiency by 0.5% for the hollow-cone injector at the NO_X limit.
9. High swirl significantly altered the fuel distribution for fuel-stratified conditions. The images showed low ϕ in the central region, even for SOI with significant NO_X production. Thus, they indicated that the high swirl causes the higher ϕ regions to be shifted radially outward compared to the low-swirl case.
10. Decreasing the injection pressure to 70 bar reduced the combustion efficiency at the NO_X limit by 1% for the hollow-cone injector, and by 1.5% for the 8-hole injector.
11. Increasing the injection pressure from 120 bar to 170 bar increased the combustion efficiency by 0.5% at the NO_X limit for the 8-hole injector. This was a 3.5% increase over the hollow-cone injector base case, and represents a very substantial overall improvement in combustion efficiency from 64% (without fuel stratification) to 92.5% at the NO_X limit.
12. Improvements in low-load combustion efficiency correlated strongly with fuel injection timing. The later the fuel could be injected with NO_X levels still below the limit, the higher the combustion efficiency. We hypothesize that this is because, with later injection, the formation of the fuel distribution is dominated by the fuel-injection process, with less time for in-cylinder turbulence to transport fuel out of the main fuel pockets to form overly lean regions.

The results of this investigation indicate that the ideal fuel distribution for low-load HCCI combustion would be a “top-hat profile” in ϕ. The mixture should be stratified such that lean regions have near-zero fuel and regions with fuel have a ϕ higher than 0.2, so combustion reaches completion and combustion efficiency is maximized. The richest regions should have a ϕ smaller than 0.6 in order not to create NO_X. Spatial and statistical fuel distribution measurements can be used to predict combustion efficiency and NO_X, assuming all of the fuel throughout the cylinder is measured. This can help verify and improve spray models, provide insight into in-cylinder combustion processes, and possibly guide future engine development.

ACKNOWLEDGEMENTS

The authors would like to thank the following people from Sandia National Laboratories for their help with this study: Sal R. Birtola for his considerable help with the design of the optical engine and acquisition of the machined parts; Kenneth St. Hilaire, Lloyd Claytor, David Cicone, and Eldon Porter for assembling and maintaining the optical engine; Christopher Carlen for help with the engine-control and camera-synchronization electronics; and Gary Hubbard for help with the data acquisition system and programming support.

This work was performed at the Combustion Research Facility, Sandia National Laboratories, Livermore, CA. Support was provided by the U.S. Department of Energy, Office of FreedomCAR and Vehicle Technologies. Sandia is a multiprogram laboratory operated by the Sandia Corporation, a Lockheed Martin Company, for the United States Department of Energy's National Nuclear Security Administration under contract DE-AC04-94AL85000.

REFERENCES

1. Dec, J. E. and Sjöberg, M., “Isolating the Effects of Fuel Chemistry on Combustion Phasing in an HCCI Engine and the Potential of Fuel Stratification for Ignition Control,” SAE paper 2004-01-0557, 2004.
2. Dec, J.E., “A Computational Study of the Effects of Low Fuel Loading and EGR on Heat Release Rates and Combustion Limits in HCCI Engines,” SAE paper 2002-01-1309, 2002.
3. Dec, J. E. and Sjöberg, M., “A Parametric Study of HCCI Combustion – the Sources of Emissions at Low Loads and the Effects of GDI Fuel Injection,” SAE paper 2003-01-0752, 2003.
4. Sjöberg, M. and Dec, J. E., “Combined Effects of Fuel-Type and Engine Speed on Intake Temperature Requirements and Completeness of Bulk-Gas Reactions in an HCCI Engine,” SAE paper 2003-01-3173, 2003.
5. Sjöberg, M. and Dec, J. E., “An investigation into lowest acceptable combustion temperatures for hydrocarbon fuels in HCCI engines,” *Proc. Combust. Inst.,* Vol. 30, pp. 2719 – 2726, 2005.
6. Jun, D. and Iida, N., “A Study of High Combustion Efficiency and Low CO Emission in a Natural Gas HCCI Engine,” SAE Paper 2004-01-1974, 2004.
7. Aroonsrisopon, P. W., Werner, P., Waldman, J. O., Sohm, V. and Foster, D. E., Morikawa, T., Minoru, I., “Expanding the HCCI Operation with the Charge Stratification,” SAE paper 2004-01-1756, 2004.

8. Sjöberg, M., Edling, L.-O., Eliassen, T., Magnusson, L., and Ångström, H.-E., "GDI HCCI: Effects of Injection Timing and Air Swirl on Fuel Stratification, Combustion and Emissions Formation," SAE paper 2002-01-0106, 2002.
9. Hultqvist A., Christensen, M., Johansson, B., Richter, M., Nygren, J. Hult, H. and Aldén, M., "The HCCI Combustion Process in a Single Cycle – High-Speed Fuel Tracer LIF and Chemiluminescence Imaging," SAE paper 2002-01-0424, 2002.
10. Thirouard, B., Cherel, J. and Knop, V., "Investigation of Mixture Quality Effect on CAI Combustion," SAE paper 2005-01-0141, 2005.
11. Reuss, D. L. and Sick, V., "Inhomogeneities in HCCI Combustion: An Imaging Study," SAE paper 2005-01-2122, 2005.
12. Hultqvist, A., Christensen, M., Johansson, B., Franke, A., Richter, M., and Aldén, M., "A Study of the Homogeneous Charge Compression Ignition Combustion Process by Chemiluminescence Imaging," SAE paper 1999-01-3680, 1999.
13. Kumano, K. and Iida, N., "Analysis of the Effect of Charge Inhomogeneity on HCCI Combustion by Chemiluminescence Measurement," SAE paper 2004-01-1902, 2004.
14. Dec, J. E., Hwang, W., and Sjöberg, M., "An Investigation of Thermal Stratification in HCCI Engines using Chemiluminescence Imaging," SAE paper 2006-01-1518, 2006.
15. Richter, M., Engström, J., Franke, A., Aldén, M., Hultqvist, A., and Johansson, B., "The Influence of Charge Inhomogeneity on the HCCI Combustion Process," SAE paper no. 2000-01-2868, 2000.
16. Steeper, R., De Zilwa, S., and Fayoux, A., "Coevaporative Tracer-PRF Mixtures for LIF Measurements in Optical HCCI Engines," SAE paper 2005-01-0111, 2005.
17. Han, D. and Steeper, R. R., "Examination of Iso-octane/Ketone Mixtures for Quantitative LIF Measurements in a DISI Engine," SAE paper 2002-01-0837, 2002.
18. Schulz, C. and Sick, V., "Tracer-LIF diagnostics: quantitative measurement of fuel concentration, temperature and fuel/air ratio in practical combustion systems," *Prog. Energy Combust. Sci.*, Vol. 31, pp. 75 – 121, 2005.
19. De Zilwa, S. and Steeper, R., "Predicting Emissions from HCCI Engines using LIF Imaging," SAE paper 2005-01-3747, 2005.
20. De Zilwa, S. and Steeper, R., "Predicting NO_X Emissions from HCCI Engines Using LIF Imaging," SAE paper 2006-01-0025, 2006.
21. Steeper, R. R. and De Zilwa, S., "Improving the NO_X-CO_2 Trade-Off of an HCCI Engine Using a Multi-Hole Injector," SAE paper 2007-01-0180, 2007.
22. Heywood, J. B., Internal Combustion Engine Fundamentals, McGraw-Hill, New York, 1988.
23. Koban, W., Koch, J. D., Hanson, R. K., and Schulz, C., "Absorption and fluorescence of toluene vapor at elevated temperatures," *Phys. Chem. Chem. Phys.*, Vol. 6, pp. 2940-2945, 2004.
24. Hwang, W. and Dec, J. E., "A Laser-Induced Fluorescence Diagnostic for Measuring Fuel and Corresponding Temperature Distributions in Direct-Injection Internal Combustion Engines," to be submitted to *Appl. Phys. B*, 2007.
25. Sjöberg, M. and Dec, J. E., "An Investigation of the Relationship between Measured Intake Temperature, BDC Temperature, and Combustion Phasing for Premixed and DI HCCI Engines," SAE Paper 2004-01-1900, 2004.
26. VanDerWege, B. A. and Hochgreb, S., "Effects of Fuel Volatility and Operating Conditions on Fuel Sprays in DISI Engines: (1) Imaging Investigation," SAE Paper 2000-01-0535, 2000.
27. Christensen, M., Hultqvist, A., and Johansson, B., "The effect of top-land geometry on emissions of unburned hydrocarbons from a homogeneous charge compression ignition (HCCI) engine," SAE paper 2001-01-1893, 2001.
28. Aceves, S. M., Flowers, D. L., Espinosa-Loza, F., Martinez-Frias, J., Dibble, R. W., Christensen, M., Johansson, B., and Hessel, R. P., "Piston-Liner Crevice Geometry Effect on HCCI Combustion by Multi-Zone Analysis," SAE paper 2002-0-2869, 2002.
29. Hwang, W., Dec, J. E., and Sjöberg, M., "Spectroscopic and Chemical-Kinetic Analysis of the Phases of HCCI Autoignition and Combustion for Single- and Two-Stage Ignition Fuels," submitted to *Combust. Flame*, 2007.